JACS
JOURNAL OF THE AMERICAN CHEMICAL SOCIETY
pubs.acs.org/JACS
Article

# Chemical Insights into the Formation of Colloidal Iridium Nanoparticles from In Situ X-ray Total Scattering: Influence of Precursors and Cations on the Reaction Pathway

Jette K. Mathiesen,[¶] Jonathan Quinson,*,[¶] Sonja Blaseio, Emil T. S. Kjær, Alexandra Dworzak, Susan R. Cooper, Jack K. Pedersen, Baiyu Wang, Francesco Bizzotto, Johanna Schröder, Tiffany L. Kinnibrugh, Søren B. Simonsen, Luise Theil Kuhn, Jacob J. K. Kirkensgaard, Jan Rossmeisl, Mehtap Oezaslan, Matthias Arenz, and Kirsten M. Ø. Jensen*

Cite This: https://doi.org/10.1021/jacs.2c10814
Read Online

ACCESS | Metrics & More | Article Recommendations | Supporting Information

**ABSTRACT:** Iridium nanoparticles are important catalysts for several chemical and energy conversion reactions. Studies of iridium nanoparticles have also been a key for the development of kinetic models of nanomaterial formation. However, compared to other metals such as gold or platinum, knowledge on the nature of prenucleation species and structural insights into the resultant nanoparticles are missing, especially for nanoparticles obtained from $Ir_xCl_y$ precursors investigated here. We use *in situ* X-ray total scattering (TS) experiments with pair distribution function (PDF) analysis to study a simple, surfactant-free synthesis of colloidal iridium nanoparticles. The reaction is performed in methanol at 50 °C with only a base and an iridium salt as precursor. From different precursor salts—$IrCl_3$, $IrCl_4$, $H_2IrCl_6$, or $Na_2IrCl_6$—colloidal nanoparticles as small as $Ir_{\sim 55}$ are obtained as the final product. The nanoparticles do not show the bulk iridium face-centered cubic (*fcc*) structure but show decahedral and icosahedral structures. The formation route is highly dependent on the precursor salt used. Using $IrCl_3$ or $IrCl_4$, metallic iridium nanoparticles form rapidly from $Ir_xCl_y^{n-}$ complexes, whereas using $H_2IrCl_6$ or $Na_2IrCl_6$, the iridium nanoparticle formation follows a sudden growth after an induction period and the brief appearance of a crystalline phase. With $H_2IrCl_6$, the formation of different $Ir_n$ ($n$ = 55, 55, 85, and 116) nanoparticles depends on the nature of the cation in the base (LiOH, NaOH, KOH, or CsOH, respectively) and larger particles are obtained with larger cations. As the particles grow, the nanoparticle structure changes from partly icosahedral to decahedral. The results show that the synthesis of iridium nanoparticles from $Ir_xCl_y$ is a valuable iridium nanoparticle model system, which can provide new compositional and structural insights into iridium nanoparticle formation and growth.

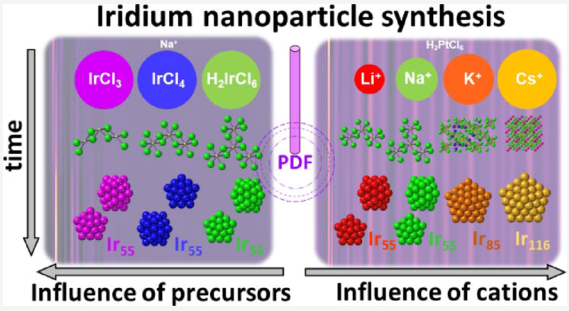


## 1. INTRODUCTION

Understanding the formation of nanomaterials is an intense and rewarding area of research.[1−5] By understanding how nanomaterials form, a better control of their synthesis can be achieved, which ultimately allows tuning and optimizing their physicochemical properties for a given application. In the past decades, the development and increasing accessibility of characterization tools, such as transmission electron microscopy (TEM),[6] small angle X-ray scattering (SAXS),[7] or X-ray absorption spectroscopy (XAS),[8,9] with the opportunities to perform *in situ* studies[10] have provided new insights into the formation of nanomaterials,[11] for example, for the formation of supported nanomaterials in the solid phase.[12,13] However, wet-chemical methods performed in a solvent are also widely used to prepare nanomaterials due to their tractability, and wet-chemical colloidal syntheses have indeed already largely contributed to advancing various research fields.[14,15] Understanding the formation of nanomaterials in liquids remains challenging[16] due to the complex interplay between the chemicals needed as precursors,[17] solvent,[18,19] ligands,[19] reducing agents,[20] and parameters, such as temperature, pH, pressure, etc. The exact process(es) of formation of nanomaterials in the liquid phase, e.g., from molecular metal ion precursors of precious metals to nanomaterials comprising hundreds or thousands of atoms, is therefore still debated and refined.[16,17,21,22]

The formation of precious metal nanoparticles (NPs) such as gold (Au) or platinum (Pt), that are key in multiple applications,

Received: October 12, 2022

Downloaded via COPENHAGEN UNIV LIBRARY on January 15, 2023 at 11:34:47 (UTC).
See https://pubs.acs.org/sharingguidelines for options on how to legitimately share published articles.

has been extensively studied.[7,17] For other systems such as iridium (Ir) NPs, there is a lack of understanding of the formation at the molecular and atomic level.[23] An exception to this statement is the case of $Ir(0)_n$ stabilized by polyoxoanions where nucleation, for example, is defined at the near-atomic level.[24] However, for Ir NPs formed from $Ir_xCl_y$ precursors, e.g., with alcohols as reductants, the prenucleation species, the specific Ir-based intermediates or products formed are still not well understood and there is virtually no knowledge of the resulting structures. This lack of knowledge is at first surprising for two reasons. First, Ir is a relevant material for multiple applications,[23,25] including heterogeneous catalysis.[26,27] Ir has also found applications in sensing[28] or medicine,[29,30] both as monoatomic, or within multimetallic materials.[23] Ir NPs are also increasingly studied for energy conversion, in particular as catalyst for the oxygen evolution reaction.[23,28,31] Second, Ir NPs have been a model system used for development of kinetic models of nanomaterial formation.[23] In particular, Finke and co-workers have done extensive, seminal work on $Ir_{\sim 300}$ clusters stabilized by a polyoxoanion and tetrabutyl ammonium cations to develop and refine the so-called Finke−Watzky kinetic-based autocatalytic model.[22,24,32,33] Finke and co-workers have over several years studied the influence of numerous parameters and tested different models, for which an account is given in a recent review.[23] Based on experimentally identified key pseudo-elementary steps, a slow and continuous nucleation followed by an autocatalytic surface growth is key to explain the formation of Ir NPs.[24,34] Recently, it was shown that the narrow size distribution observed for Ir NPs can be explained by different kinetics of growth where smaller NPs grow faster than large ones.[22] Further understanding of the causes of this phenomenon for various Ir NP syntheses on a molecular or atomic level would be a key achievement to refine and build additional structural insights into models for NP formation.

The formation of nanomaterials in solution is often described by the classical nucleation theory (CNT)[16] where seeds are first formed in a nucleation step followed by the growth of the seeds to NPs. However, identifying the seeds with often a short lifetime remains an experimental challenge, and studies driven by computational approaches generally rely on assumptions on the species present and formed during nucleation.[22] The CNT and its framework are therefore regularly challenged. For instance, recent work on $Ir_n$ disproved the applicability of the CNT.[24,34] The possible existence of "prenucleation clusters" (PNCs) has in the past decade led to a large number of studies investigating the chemistry and interactions of the compounds and clusters formed before nucleation.[35−38] However, the structure and role of the prenucleation species on the material formation pathway is still not clear. To achieve a more detailed understanding of nanomaterial formation, ultimately to fully master the design of NPs, it is crucial to obtain more experimental evidence on the nature of the species formed during synthesis.

Here, we investigate the structural changes taking place during the formation of Ir NPs in a simple colloidal synthesis. Colloidal synthesis methods generally rely on the use of additives, such as surfactants,[39] polymers,[40] polyoxanions,[41] or ionic liquids,[26] and it is challenging to assess the effect(s) of these additives in the formation of NPs. We overcome these challenges using a surfactant-free synthesis of Ir NPs[42] that can be performed at high metal concentration of 100 mM,[43] which makes it compatible with *in situ* X-ray total scattering (TS) experiments with pair distribution function (PDF) analysis[44] to gain new insights into the structural chemistry of Ir NP formation. We first report the formation of surfactant-free Ir NPs in alkaline methanol (MeOH) using different precursors, e.g., $IrCl_3$, $IrCl_4$, and $H_2IrCl_6$. We show that even small modifications to the synthesis procedure, such as changing $IrCl_3$ or $IrCl_4$ for $H_2IrCl_6$, change the overall formation pathway and lead to a transient crystalline phase that appear to induce a burst-growth-like phenomenon.[33,45] We then show that the cation of the base added also heavily affects the reaction pathway and the resulting size of the Ir NPs. The NPs formed herein do not take the bulk face-centered cubic (*fcc*) structure but are decahedral and icosahedral clusters whose size (from $Ir_{\sim 55}$ to $Ir_{\sim 116}$) depends on the synthesis conditions.

## 2. MATERIALS AND METHODS

**2.1. Iridium NP Synthesis.** The NP synthesis was performed following a previously reported method.[42,43,46] A solution containing either $IrCl_3{\cdot}xH_2O$ (99.9%, Alfa Aesar), $IrCl_4$ (99.9%, Alfa Aesar), $H_2IrCl_6{\cdot}H_2O$ (99.9%, Aldrich), or $Na_2IrCl_6{\cdot}6H_2O$ (99.9% trace metals basis) as metal ion precursor in alkaline LiOH (anhydrous 98%, Alfa Aesar), NaOH (98%, Alfa Aesar), KOH ($KOH{\cdot}xH_2O$, ≥99.995%, Fluka), or CsOH (99.95%, Aldrich) in methanol (MeOH, ≥99.9%, HiPerSolv CHROMANORM, VWR) was obtained by mixing a stock solution of the metal ion precursor with a solution of the base of interest in MeOH. To obtain a high enough scattering signal for PDF analysis, the final concentration of metal ion precursor was 100 mM and 1 M base. The solution was then heated to 40 or 50 °C as noted for each experiment.

**2.2. Data Acquisition for X-ray TS Experiments.** The X-ray TS experiments were conducted in a custom-made setup for *in situ* studies provided by the 11-ID-B beamline, APS, Argonne National Laboratory (see Figure S1). This setup is composed of an aluminum block with cut out slots where glass tubes designed for nuclear magnetic resonance (NMR) can be vertically placed (Wildmad, 3 mm outer diameter, 0.27 mm wall thickness, Type 1 Class A). The precursor solution was injected into the NMR tube. The temperature was monitored using a thermocouple, which was placed in an NMR tube with a NaCl powder standard. TS data were collected in transmission geometry using a Perkin-Elmer flat panel detector with a pixel size of 200 × 200 $\mu$m. A wavelength of 0.2114 Å was used, and the sample-to-detector distance was calibrated using a NaCl powder standard. The 2D data were integrated using GSAS-II and Fit2D.[47−49] TS data for the precursor solutions were collected for 10 min at room temperature before initiation of heating. The solutions were then heated to 50 °C (alternatively 40 °C) at a rate of 5 °C $min^{-1}$ while collecting TS data with a time resolution of 30 s.

We note here that exposure of a sample to an X-ray beam may cause beam damage due to X-ray absorption. At this point, we cannot address whether the beam has any influence on the Ir NP formation but note that the high X-ray energy (58.6 keV) used for TS measurements reduces X-ray absorption and thus beam damage effects.

**2.3. PDF Analysis.** The X-ray TS data were Fourier transformed to obtain the PDFs using xPDFsuite with a $Q_{max}$ of 18 $Å^{-1}$.[50] The background subtraction was performed by subtracting the scattering signal obtained from an identical experiment performed without the metal ion precursor present. Modeling of PDFs was done using DiffPy-CMI[51] as described in further detail in Section 1 of the Supporting Information (SI).

**2.4. Further Characterization.** We furthermore conducted XAS, SAXS, TEM, Fourier transform infrared (FTIR) spectroscopy, and gas chromatography coupled to mass spectrometry (GCMS) experiments, as well as density functional theory (DFT) calculations. Details on these experiments and methods are given in Section 1 of the SI.

## 3. RESULTS AND DISCUSSION

**3.1. General Equations of the Reactions.** Before presenting data and results from our experiments, we discuss


https://doi.org/10.1021/jacs.2c10814
J. Am. Chem. Soc. XXXX, XXX, XXX−XXX

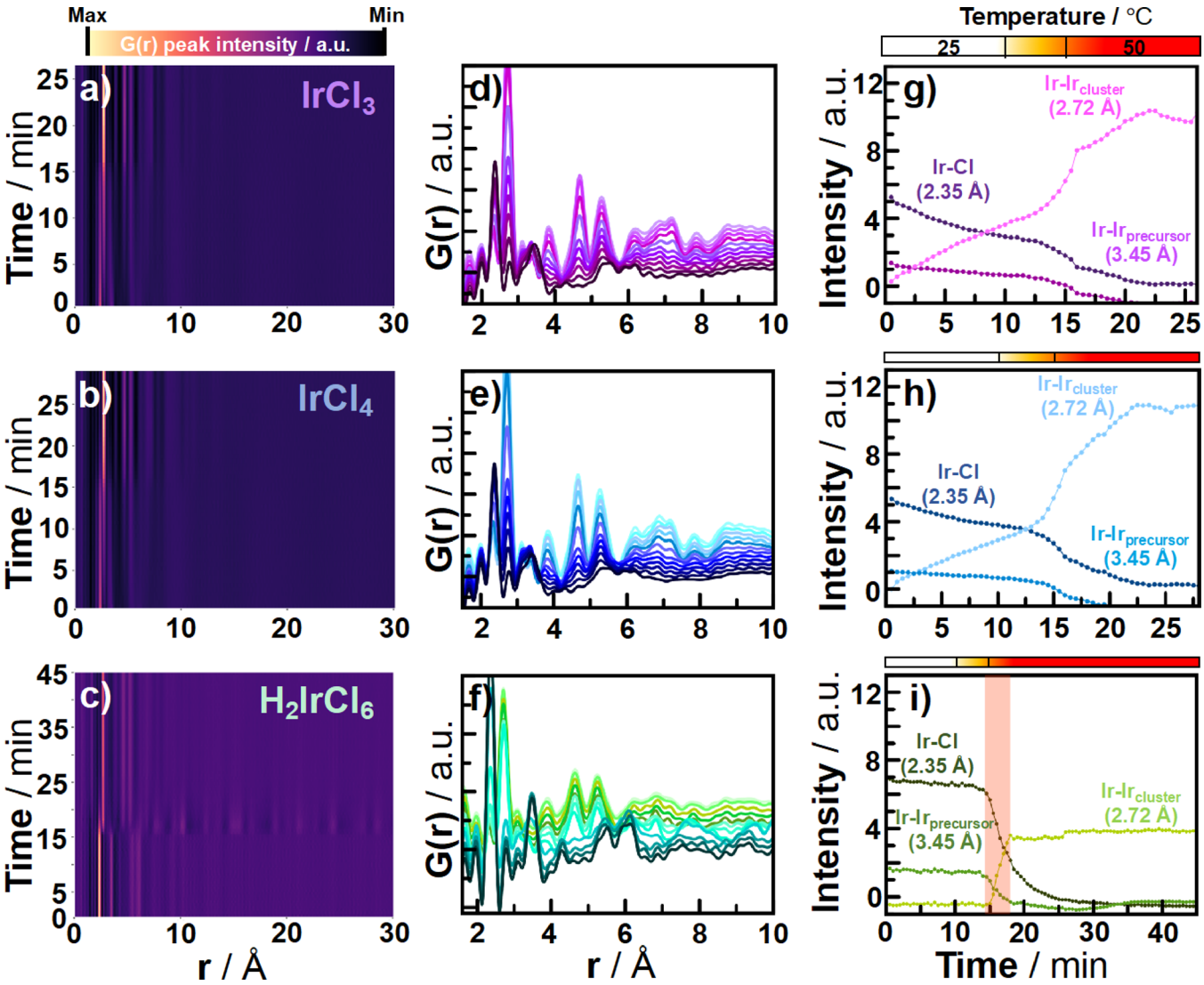


**Figure 1.** (a−c) Experimental *in situ* X-ray TS data following the formation of Ir NPs from (a) $IrCl_3$, (b) $IrCl_4$, and (c) $H_2IrCl_6$ as precursors presented in real space, $G(r)$. (d−f) Selected PDFs from (bottom) precursor to (top) Ir NPs from the beginning to the end of the experiments with 2.5 min time resolution. (g−i) Evolution of PDF peak intensity associated with Ir−Cl (2.35 Å), Ir−Ir in the precursor (3.45 Å), and Ir−Ir in the NPs formed (2.72 Å). Panels (a, d, and g) relate to $IrCl_3$, (b, e, and h) relate to $IrCl_4$, and (c, f, and i) relate to $H_2IrCl_6$.

the general equations of the reactions expected to take place in our $Ir_n$ NP synthesis. The formation of NPs in our synthesis method requires the precursors $IrCl_3$, $IrCl_4$, or $H_2IrCl_6$ together with MeOH and MOH (where M = Li, Na, K, or Cs). Along with $Ir_n$ NPs, the main products of the reactions are thus likely $M^+$, $Cl^-$, $H_2O$, as well as oxidation products from MeOH.[18] The oxidation can lead to different species, e.g., aldehydes, carboxylates, and possibly alkoxides as suggested elsewhere as key reducing agents.[52] As it will be discussed further below, we expect here $CO_2$ and CO as products. These species are very likely to stabilize the surfactant-free NPs. Previous Zeta-potential analysis of Pt NPs[18] from a closely related synthesis suggests the presence of stabilizing negatively charged species on the NP surface, and $CO_{ad}$ is also expected to serve as stabilizer on the Ir NP surface. Moreover, due to the very close p*K*a values of MeOH (15.3) and water (15.7), most $M^+OH^-$ is actually in the form $M^+CH_3O^-$ as ion-pairs in MeOH.[53] Methoxy groups may thus also stabilize the NP surface.

If assuming that the main reactions accounting for the reduction and stabilization of the Ir NPs are (1) deprotonation of $CH_3OH$, (2) reduction of $Ir^{3+}$ or $Ir^{4+}$ to Ir(0) through oxidation of $CH_3OH$ to $CO_2$, (3) reduction of $Ir^{3+}$ or $Ir^{4+}$ to Ir(0) through oxidation of $CH_3OH$ to CO, and (4) stabilization of Ir NPs by $Cl^-$, CO, and $CH_3O^-$, the overall reaction for the precursor salts can be summarized as

$$\begin{aligned}&(x+y)\,IrCl_3 + \left(\frac{x}{2}+\frac{3y}{4}+z\right)CH_3OH + (3x+3y+z)\,NaOH\\&\rightarrow [\mathbf{Ir}_{x+y}(\mathbf{Cl})_a(\mathbf{CO})_b(\mathbf{CH_3O})_c]^{-(a+c)} + \frac{x}{2}CO_2 + \left(\frac{3y}{4}-b\right)CO\\&+\left(\frac{5x}{2}+3y+z\right)H_2O + (3x+3y-a)\,Cl^- + (3x+3y+z)\,Na^+\\&+(z-c)\,CH_3O^-\end{aligned}$$

for the example of the reduction of $IrCl_3$. Details on balancing these equations are given in Section 2 of the SI together with the related equations when $IrCl_4$ and $H_2IrCl_6$ are used as precursors. We can thus describe the product as $[Ir_n(Cl)_a(CO)_b(CH_3O)_c]^{-(a+c)}$. As we will discuss below in Sections 3.3 and 3.6, our experiments show that $n$ can be controlled to the values $n \sim 55$, 86, or 116 by carefully


https://doi.org/10.1021/jacs.2c10814
J. Am. Chem. Soc. XXXX, XXX, XXX−XXX

controlling the reaction conditions. However, the PDF, extended X-ray absorption fine structure (EXAFS), and DFT analysis performed here do not allow us to address which species may be present on the surface of the NPs and thus evaluate *a*, *b*, or *c*. For the X-rays based techniques, this is due to the limited X-ray scattering power of O and C compared to Ir. We will therefore refrain to claim here any full reaction mechanism and only focus on the structural changes related to the Ir precursors and products in the synthesis.[11,54] For simplicity, we will also not further use the description of the products as $[Ir_n(Cl)_a(CO)_b(CH_3O)_c]^{-(a+c)}$ but refer to the surfactant-free Ir NPs as $Ir_n$. The species that might account for the stabilization of the $Ir_n$ NPs have not been considered at this stage in PDF, XAS, or DFT modeling and fitting.

Note that in the reactions presented above, we have not taken into account the possible role of $M^+$ cations and possibly $H^+$ cations in NP stabilization although this may take place. In particular, it has recently been suggested that Ir−H hydrides are likely intermediates in the formation of Ir NPs.[24] Although there is at this stage no definite proof of their formation for the synthesis used here, they could come into play via the reaction:

$$H_2CO + Ir_n \rightarrow H - Ir_n - CHO \rightarrow H_2Ir_nCO$$

where $H_2CO$ is an oxidation product of MeOH, which is consistent with the observation of $CO_{ad}$ species as detailed below.

**3.2. Influence of Metal Precursor Salts on the Ir NP Formation Pathway.** *3.2.1. Trends.* Uncovering how the synthetic parameters influence the characteristics and properties of Ir NPs is essential to ultimately control nanomaterial shape, size, and structure. We therefore start by gaining an overview of the effect(s) of different metal ion precursors with different oxidation degrees on the reaction process and end products using $IrCl_3$, $IrCl_4$, or $H_2IrCl_6$ as precursor salts. Figure 1a−c shows PDFs obtained from experimental X-ray TS data collected during Ir NP syntheses at 50 °C. Selected PDFs are shown in Figure 1d−f. The disappearance and appearance of specific interatomic distances describe well the reduction and Ir NP formation processes, occurring during the synthesis. At the beginning of all of the three experiments, a strong peak at 2.35 Å can be assigned to the nearest-neighbor Ir−Cl bond in the precursor structure (see Figure S2a for representation of the peak origin in the structure).[55] At the end of the experiments, a strong peak representing the nearest-neighbor metallic Ir−Ir bond with a distance of 2.72 Å is present, confirming the formation of metallic Ir NPs (Figure S2b).[56] These results are confirmed by XAS, see Section 2.3 in SI. A closer look at selected PDFs in Figure 1d−f also shows a third intense PDF peak from the precursor structure (i.e., 0 min into the experiment) at 3.45 Å. The distance at 3.45 Å can be assigned to an Ir−Ir distance in the precursor structure if assuming edge-sharing octahedral coordination, revealing that the precursor clusters formed in the solution are larger than, e.g., isolated Cl- or O-coordinated Ir monomers (see Figures S2a and S3 for enhanced view of the peak changes at 3.45 Å).

*3.2.2. The Cases of $IrCl_3$ and $IrCl_4$.* While the three PDF peaks discussed are present using both $IrCl_3$, $IrCl_4$, or $H_2IrCl_6$ as precursors, the evolution of the peak intensity reveals different kinetics of NP formation for the different precursors. We first consider the experiments performed with $IrCl_3$ and $IrCl_4$. As seen in Figure 1g,h, the formation of Ir NPs from the precursors involves a gradual decrease of the precursor Ir−Cl and Ir−Ir PDF peak intensity (denoted Ir−Cl and $Ir-Ir_{precursor}$, respectively, in Figure 1g,h) and a gradual increase in the metallic Ir−Ir peak intensity (denoted $Ir-Ir_{cluster}$). This behavior reveals that a continuous reduction and the formation of Ir NPs take place while using the metallic Ir−Ir peak as a proxy for the formation of Ir NPs. The formation of Ir NPs accelerates over time when the temperature reaches 50 °C. However, we also note that the metallic Ir−Ir PDF peak is observed almost from the beginning of the reaction and its peak intensity shows a continuous increase even at 25 °C. The presence of Ir−Ir bonds from the beginning of the reaction agrees with partial reduction of Ir precursor ions observed by X-ray absorption near edge structure (XANES) in presence of a base, see Figure S4. At the end of the experiment, the precursor Ir−Cl and Ir−Ir PDF peaks have completely disappeared, which supports a full conversion of the initial precursor complex structure into Ir NPs during the *in situ* experiments. Although a detailed kinetics study would be challenging here due to the change of temperature during the precursor consumption and NP formation, the observed peak intensity trends would be compatible with the expected reduction and autocatalytic growth described by a three-step kinetic model.[22,57] Furthermore, the size distribution of ca. ±15% for the near monodisperse NPs obtained here is also consistent with the operation of that mechanism.

*3.2.3. The Case of $H_2IrCl_6$.* In contrast to $IrCl_3$ and $IrCl_4$, the formation of Ir NPs from $H_2IrCl_6$ follows a significantly different process as illustrated in Figure 1i. While the system seems to be in an induction phase, where no changes occur until ca. 15 min into the experiment, a behavior compatible with a burst-growth mechanism[45] is observed. Here, the intensity of the Ir−Ir peak, characteristic of metallic NPs, suddenly increases when the temperature reaches 50 °C and quickly reaches a steady value. Meanwhile, the peaks related to the precursor decrease. Although our data unfortunately do not allow a detailed kinetic analysis, this behavior would be compatible with a four-step double autocatalytic kinetic model more commonly used to describe Pt NP formation.[17,58] These results are reproducible, Figure S8, and also observed at a lower temperature (i.e., 40 °C), Figure S9. The induction period, where no new PDF peaks appear, may be related to a phase in the reaction where the precursor gets reduced as assessed from XANES experiments, Figure S4. An additional surprising feature is observed when $H_2IrCl_6$ is used as precursor. Just as the metallic Ir structure begins to form in the sudden burst-growth event (i.e., 15 min into the experiment), a transient crystalline structure with long-range atomic order emerges. We only observe this crystalline phase when $H_2IrCl_6$ is used as the precursor. The transient crystalline phase is clearly observed in the PDFs in Figure 1c and the corresponding *Q*-space data in Figure S10c, showing clear Bragg peaks. The transient crystalline phase is present for ca. 5 min (from time-point 15 to 20 min into the experiment), whereafter it vanishes and Ir NPs form. Interestingly, this area coincides with the point during synthesis where the peaks related to the precursor decrease and the metallic Ir−Ir peak intensity rapidly increases: the area highlighted in red in Figure 1i. The same crystalline phase was observed to form also in the experiment performed at lower temperature (40 °C). Here, the lifetime of the crystalline phase was observed to extend throughout the experiment, Figure S9.

*3.2.4. Discussion.* The similarities in behavior between $IrCl_3$ and $IrCl_4$ and the differences to the experiment with $H_2IrCl_6$ can be at first surprising. Ir in $IrCl_4$ and $H_2IrCl_6$ are expected to be in the same oxidation state IV, while it is III in $IrCl_3$. It could thus be expected that the reduction of the precursors with $Ir^{IV}Cl_4$ or


https://doi.org/10.1021/jacs.2c10814
J. Am. Chem. Soc. XXXX, XXX, XXX−XXX

$H_2Ir^{IV}Cl_6$ would follow the same trends but would be different for $Ir^{III}Cl_3$. XANES analysis (Figure S4) of the precursor solutions shows that Ir in $IrCl_3$ solutions is indeed more reduced than Ir in $IrCl_4$ and $H_2IrCl_6$ solutions although we also observed a slightly lower oxidation degree for $IrCl_4$ than $H_2IrCl_6$ in solution. However, to explain the apparent different formation routes of Ir NPs, *the geometry of the starting complex seems to matter more than its oxidation degree* as it will be discussed further below. The dependence of the formation route on experimental parameters such as precursors is in line with previous results on $Ir_n$ NPs although very different model systems were used.[24,34]

**3.3. Size and Structure of $Ir_n$ NPs from Different Metal Precursors.** *3.3.1. Size of the Final $Ir_n$ NPs.* Before addressing the nature of the precursors present in solution, we examine the size and structure of the final product of the reactions. SAXS analysis of the final synthesis product reveals Ir NPs with a size of ca. 1.3 nm, which agrees with TEM characterization, see Table 1 and Figure S11. The lack of influence of the precursors on the NP size between the three syntheses is in agreement with previous reports using UV−vis synthesis,[59] and the size observed is consistent with 1.1−1.6 nm obtained at lower precursor concentration.[46,59,60] It is also consistent with the small size of Ir NPs obtained by other surfactant-free syntheses.[40,61] The resulting sizes thereby show that despite using a surfactant-free synthesis, small-sized NPs can be easily obtained. For this size range, $Ir_{55-150}$ NPs are expected to form,[57] i.e., smaller than the typical $Ir_{\sim 300}$ obtained by Finke and co-workers in presence of a polyoxoanion that is typically larger than 2 nm.[22]

**Table 1. Size Evaluated by TEM for Different Experimental Conditions**[a]

| precursor | $IrCl_3$ | $IrCl_4$ | $H_2IrCl_6$ |
|---|---|---|---|
| size after *in situ* X-ray TS experiments/nm | 1.3 ± 0.2 | 1.2 ± 0.3 | 1.3 ± 0.3 |

[a]The size distributions are given in Figure S12.

*3.3.2. Structure of the Final $Ir_n$ NPs.* Since bulk Ir is a *fcc* metal, it could be expected that the structure of the final NPs is *fcc*.[56] However, using a Ir *fcc* model for the refinement does not account for the observed PDFs of the final NP products, see Figure 2a−c. Details on the refinement are given in Section 1 in SI, and refined parameters can be found in Table S3. While the first two nearest-neighbor Ir−Ir distances at 2.72 and 3.85 Å are fully described by a *fcc* structure model, discrepancies are found at higher *r* values in real space. In particular, a pronounced second peak at 5.20 Å in the experimental data is not taken into account and we therefore look toward other atomic structure models.

*3.3.3. Cluster Mining and PDF Fitting Using Non-fcc Structures.* It is well known that small metallic NPs are likely to take, e.g., multitwinned structures as proposed for Au NPs by Ino and Ogawa,[62] or the Marks decahedron structure proposed by Marks and Smith.[63−65] While the growth of icosahedral structures is described by the addition of a discrete number of atoms in a shell-like pattern (13, 55, 147, etc.[66]), decahedral structures can evolve along three main axes, which eventually forms different sizes and shapes of NPs with the fivefold symmetry maintained. In addition to the regular or Marks decahedron, which incorporates reentrant surfaces at the twin boundaries between adjoining single crystals (for further details, see Section 2.9 in SI), elongation perpendicular to the plane can form the so-called Ino decahedron.[67,68] To investigate the possibility of forming decahedral and icosahedral Ir NPs, a "cluster mining" approach as introduced by Banerjee et al.[69] was applied using the ASE software package.[69,70] Here, icosahedral NPs of discrete sizes were introduced in the analysis by varying the amount of atomic "shells" in the NPs, while decahedral NPs of different sizes and shapes were incorporated by varying the atomic addition along the three main axes.

The calculated PDFs of the resulting structures were fitted to the final experimental PDFs where the agreement value, $R_w$, was used to evaluate the agreement between the experimental data and the model structures. For the NPs resulting from all three metal ion precursors, the cluster mining method suggested several decahedral structures. The suggested structures included the Ino decahedral $Ir_{39}$ and $Ir_{55}$ structures to describe the final NPs. Interestingly, others have reported $Ir_{\sim 40}$ as relatively stable $Ir_n$ structures although these were obtained and stabilized for instance in zelolites[71] or with $AlEt_3$.[72] Furthermore, DFT calculations suggest that $Ir_{\sim 40-55}$ are relatively stable.[73] However, Ino decahedral $Ir_{39}$ and $Ir_{55}$ structures are difficult to distinguish through PDF analysis. This is emphasized in Figure S13a,b where comparison of calculated PDFs of different decahedral structures clearly illustrates the difficulties of separating very similarly sized structures as also shown when calculating the Pearson correlation coefficient between the PDFs (Figure S13e−g).[74] This limitation is further highlighted when using differently sized decahedral structures as models in the PDF refinement. As seen in Figure S14 and Table S6, using $Ir_{39}$ and $Ir_{55}$ as structural models provide similar $R_w$ values for refinements of the final PDF of the $H_2IrCl_6$ experiment. This stresses the limitation of solely basing structural conclusions on the PDFs. To further analyze the cluster structures suggested from the cluster mining analysis, we thus turned to DFT calculations to evaluate the stability of the proposed structures. As seen in Figure S13d, the Ino decahedral $Ir_{55}$ structure has lower energy per atom than the decahedral $Ir_{39}$, and we therefore consider the Ino decahedral $Ir_{55}$ structure for further refinements.

*3.3.4. PDF Fits with $Ir_{55}$ Models: Presence of Decahedral and Icosahedral NPs.* Figure 2d−f shows single-phase refinements using the Ino decahedral $Ir_{55}$ structure for the data set from each of the three metal ion precursors. Compared to the fit with the *fcc* model, an improvement is seen as reflected in the lower $R_w$ value, which decreases from ca. 0.35 to 0.22 for the NPs synthesized from $IrCl_3$ and $IrCl_4$. However, the Ino decahedral $Ir_{55}$ structure is not solely enough to describe the final Ir structure resulting from $H_2IrCl_6$ as metal precursor. As illustrated in Figure 2f, the relative intensities between the peaks at 4.70 and 5.20 Å cannot be fully accounted for. We therefore explore other structures. The cluster mining approach also suggested an icosahedral $Ir_{55}$ structure as a main component for the particles formed when using $H_2IrCl_6$ as metal ion precursor. Interestingly, icosahedral $Ir_{55}$ can be identified as one of the "magic-sized" Ir structures proposed by Watzky and Finke in previous work.[32,57] By introducing this structure in the refinement, the agreement with the data from the $H_2IrCl_6$ synthesis increases as seen from the lower $R_w$ value of 0.18 in Figure 2j. Including the icosahedral $Ir_{55}$ structure also gave a slightly better fit to the PDFs from $IrCl_3$ and $IrCl_4$ (Figure 2g,h) by including approx. 20−30% of the icosahedral structure. Since a larger amount of the icosahedral structure is needed to describe the NPs resulting from $H_2IrCl_6$, the NPs formed in this synthesis are more likely to display structural polymorphism.


https://doi.org/10.1021/jacs.2c10814
J. Am. Chem. Soc. XXXX, XXX, XXX−XXX

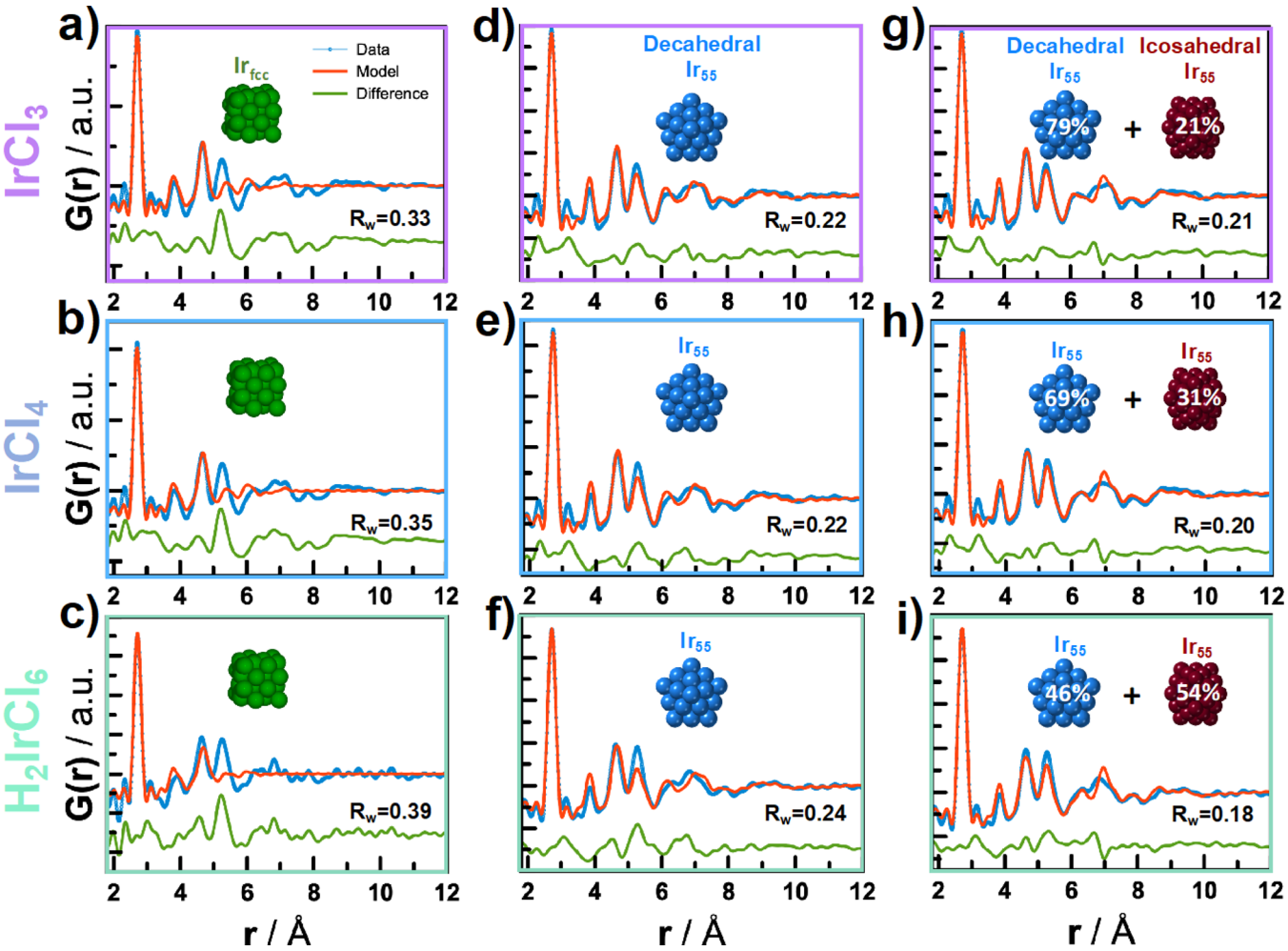


**Figure 2.** PDF refinements for Ir NPs formed at the end of the *in situ* PDF experiments (a−c) using a Ir *fcc* model with the refined values given in Table S3, (d−f) using a single-phase refinement with the Ino decahedron $Ir_{55}$ as the structure model, refined values are given in Table S4, and (g−i) when also implementing an icosahedral $Ir_{55}$ model in a two-phase refinement. The refined values are given in Table S5. The metal ion precursor is (a,d,g) $IrCl_3$, (b,e,h) $IrCl_4$, and (c,f,i) $H_2IrCl_6$. The synthesis time was ca. 25 min for $IrCl_3$ and $IrCl_4$ and ca. 40 min for $H_2IrCl_6$.

These results could be reproduced in a separate synthesis as shown in Figure S15.

Regardless of the precursor used, similarly sized $Ir_{\sim 55}$ NPs thus form and decahedral and icosahedral $Ir_{\sim 55}$ is thus considered the final product of the syntheses using the three precursors considered so far. We also note that the two-phase model is not only capable of describing the final NPs but also the NPs formed immediately after a metallic Ir−Ir distance appears. This is illustrated in Figure S16 where the time-resolved PDFs have been refined using the $Ir_{55}$ models. The refinements show that the two-phase description provides a good fit to the data soon after a metallic Ir−Ir distance appears although the presence of unreduced precursor in the beginning of the experiment leads to a lower agreement.

*3.3.5. Discussion.* We note here that the small and monodisperse NPs are obtained without surfactants, which is beneficial for high catalytic activity for, e.g., the oxygen evolution reaction for water electrolyzers.[42,46,60] Various colloidal syntheses of Ir NPs have shown to give rather small NPs.[40,61] Finke and co-workers suggested that small particles with a narrow size dispersion can be obtained because the smaller NPs grow faster than the larger ones,[22] and an open question was on the role of the polyoxoanion used as stabilizer to observe this narrow size distribution.[75] It is here shown that the same phenomenon might occur using a surfactant-free synthesis. It must be kept in mind that, as shown for a similar surfactant-free Pt NP synthesis,[18] MeOH gets oxidized during the metal reduction, see Figure S17. The related products such as $CO_{ad}$ moieties may serve as stabilizers on the Ir NP surface, see Figure S18.

**3.4. $Ir_nCl_y$ Precursor Complex Structures.** *3.4.1. Initial Species Formed.* Having established the synthesis products, we now investigate the initial precursor complex structures obtained by dissolving $IrCl_3$, $IrCl_4$, or $H_2IrCl_6$ in alkaline MeOH before formation of $Ir_n$. Elucidating the initial precursor complex structures before the formation of $Ir_n$ might provide insights into possible relations between the local ligand environment of the Ir ion in the precursor state and how the formation of NPs proceeds. This information can ultimately provide useful knowledge on the formation and role of PNCs[35] that are reported to play a role in the formation of various nanomaterials and in particular precious metal NPs.[76] However, structural knowledge of PNCs is currently very limited.

Figure 3a presents the experimental PDFs of the $IrCl_3$, $IrCl_4$, or $H_2IrCl_6$ dissolved in alkaline MeOH at room temperature. As discussed above, for all three precursors, we observed peaks that can be related to Ir−Cl bonds, Ir−Ir in edge-sharing octahedra, as well as metallic Ir−Ir bonds. The corresponding *in situ* EXAFS


https://doi.org/10.1021/jacs.2c10814
J. Am. Chem. Soc. XXXX, XXX, XXX−XXX

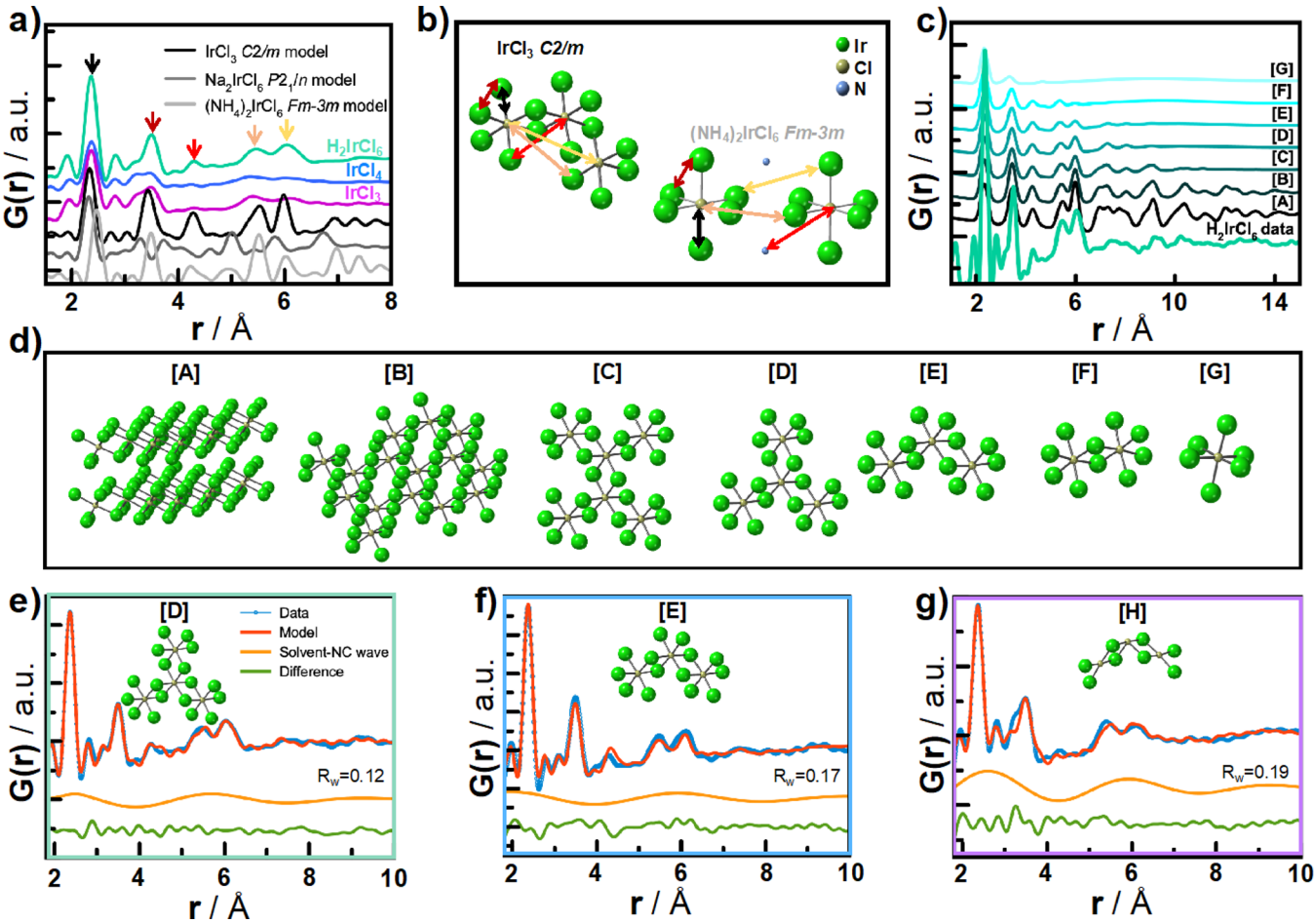


**Figure 3.** Precursor complex structures. (a) compares the experimental PDFs of the precursor complex structures obtained using $H_2IrCl_6$ (green), $IrCl_4$ (blue), and $IrCl_3$ (pink) as metal ion precursors with the $IrCl_3$ (black), $Na_2IrCl_6$ (dark gray), and $(NH_4)_2IrCl_6$ (light gray) crystal structures. The atomic pair correlations have been indicated in the $IrCl_3$ and $(NH_4)_2IrCl_6$ structures as shown in (b). (c) presents and compares the experimental PDF using $H_2IrCl_6$ with calculated PDFs for the suggested $Ir_nCl_y$ precursor complex structures as shown in (d). PDF modeling of the resulting complex from using (e) $H_2IrCl_6$, (f) $IrCl_4$, and (g) $IrCl_3$ as precursor complex structures using the models indicated.

data, Table S2, furthermore showed Ir−O bonds, which are expected to form under alkaline conditions.[77] We do not observe these directly in the PDF possibly due to the smaller scattering power of O as well as overlapping termination ripples from the limited Q-range.

To elucidate the structure of the $Ir_nCl_y^{n-}$ complexes, we compared our experimental data to calculated PDFs from the monoclinic $IrCl_3$ crystal structure (space group *C12/m1*), the $Na_2IrCl_6$ crystal structure (space group $P2_1/n$), and the $(NH_4)_2IrCl_6$ crystal structure (space group $Fm\bar{3}m$) in Figure 3a.[78−80] This comparison allows us to identify if the local structure and atomic arrangement in the bulk materials can be related to that seen in the solution structure. All three crystal structures are built from [$IrCl_6$] octahedra that are either connected by edge-sharing or isolated units. While the calculated PDFs of the $IrCl_3$ and $(NH_4)_2IrCl_6$ crystal structures illustrated in Figure 3b show features also observed in the experimental PDFs, the $Na_2IrCl_6$ structure does not show any similar features as clearly observed in Figure 3a. In particular, the peaks at 5.50 and 6.10 Å in the experimental data are not described using this model.

*3.4.2. Structural Motifs—$H_2IrCl_6$ Solution.* We start by considering the precursor complex structure resulting from $H_2IrCl_6$ in further detail. Note that in the following, we will refer to structural motives between brackets, such as [$Ir_xCl_y$], meaning that the actual related species are best described as $Ir_xCl_y^{n-}$. The PDF peak positions and relative intensities compare well to those in the local structure of the calculated PDF from $IrCl_3$, suggesting that the [$IrCl_6$] octahedra in the $H_2IrCl_6$ solution should be considered as edge-sharing rather than isolated [$IrCl_6$]. We therefore use the bulk $IrCl_3$ structure as an initial building block and "carve" out possible structures of varying lengths and coordination environments. Figure 3c shows the experimental PDF of $H_2IrCl_6$ (green) and calculated PDFs of the carved-out structures, which are presented in Figure 3d. Structure [**A**] illustrates a layered structure as seen for the bulk $IrCl_3$ structure, while [**B**] shows a single layer of the $IrCl_3$ structure. As clearly illustrated, the coherence length of structures [**A**] and [**B**] extends beyond the oscillations observed in the experimental PDF. Furthermore, the relative intensities of the two peaks at ca. 5.50 and 6.10 Å do not show the same intensity ratio as observed in the experimental PDF. Thus, the [**A**] and [**B**] structures were excluded as possible precursor clusters. Smaller single-layered structures were further investigated as illustrated in Figure 3c,d. The smaller structures were found to provide a better description; however, when reaching the di- and monomeric structures [**F**] [$Ir_2Cl_{10}$] and [**G**] [$IrCl_6$], respectively, the calculated PDFs were significantly different


https://doi.org/10.1021/jacs.2c10814
J. Am. Chem. Soc. XXXX, XXX, XXX−XXX

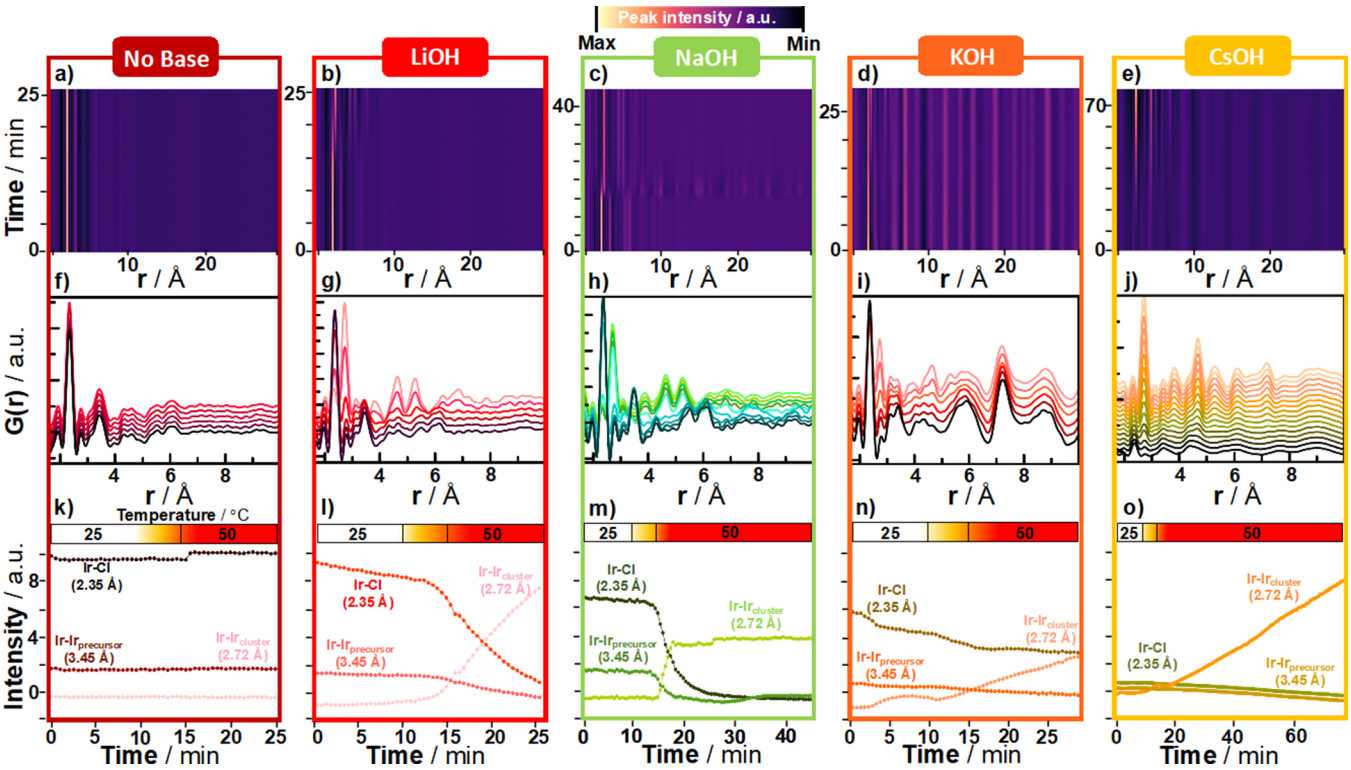


**Figure 4.** Experimental X-ray TS data following the formation of Ir NPs with different bases using $H_2IrCl_6$ as metal ion precursor in (a−e) real space, $G(r)$, where (f−j) show selected PDFs from (bottom) precursor to (top) Ir NPs from the beginning to the end of the experiments with 5-min time resolution in a limited $r$-range from 1.6 to 10 Å. (k−o) Evolution of peak intensity associated with Ir−Cl (2.35 Å), Ir−Ir in the precursor (3.45 Å), and Ir−Ir in the NPs formed (2.72 Å). The base used was (a,f,k) no base, (b,g,l) LiOH, (c,h,m) NaOH, (d,i,n) KOH, and (e,j,o) CsOH.

from the experimental PDF data. Especially, the ratio of the peaks at ca. 5.50 and 6.10 Å and the coherence length are not described correctly in [**F**] and [**G**].

Based on these observations and by comparing the Pearson correlation between the experimental PDF data and calculated PDFs of the proposed models (see Figure S19), the candidate precursor complex structures are likely to fall in between [**C**] [$Ir_6Cl_{26}$] and [**D**] [$Ir_4Cl_{18}$]. By using these models, PDF refinements were performed as shown in Figure S20−21 and Tables S8−S9. The difference curve shows an oscillating pattern, which has previously been related to solvent restructuring around the small precursor complex structures.[81,82] Incorporating a sine wave function in the fit greatly improved the fit quality as seen in Figure 3e for structure [**D**] [$Ir_4Cl_{18}$]. Since both the [**C**] [$Ir_6Cl_{26}$] and [**D**] [$Ir_4Cl_{18}$] models show a good agreement with the experimental PDF, the precursor may be composed of complexes with varying sizes ranging mainly from $Ir_4Cl_{18}^{n-}$ to $Ir_6Cl_{26}^{n-}$.

*3.4.3. Structural Motifs—$IrCl_3$ and $IrCl_4$ Solutions.* With this in mind, we turn to the precursor complex structures resulting from $IrCl_3$ and $IrCl_4$. In Figure 3a, we see that the precursor complex structures were found to exhibit less-dominating features at higher $r$ values compared to those identified in the $H_2IrCl_6$ solution. This indicates that the precursor complex structures of $IrCl_3$ and $IrCl_4$ should be described with smaller structures but still with more than two Ir atoms. The PDF resulting from using $IrCl_4$ was modeled using the [**E**] [$Ir_3Cl_{14}$] model structure, including a wave function, which provided the best agreement between data and model as seen in Figures 3f and S22 and Table S10. The [**E**] [$Ir_3Cl_{14}$] structure model was likewise used to model the PDF resulting from using $IrCl_3$ as metal ion precursor, see Figures S23c and S24c. However, a slight misfit of the peak intensity ratio at 5.50 and 6.10 Å is observed. An attempt to decrease the misfit was found by constructing a reduced version of [**E**] where Cl−Cl the Cl−Cl peak contributions at 6.10 Å could be minimized. The introduction of the reduced structure [**H**] [$Ir_3Cl_8$] led to a slightly better peak intensity ratio although the agreement factor $R_w$ was not improved as displayed in Figures 3g and S23d and Table S11. Additional PDF refinements and resulting parameters are presented in Figures S20−S24 and Tables S8−S12.

We note here that the structure models presented should be considered simple representations of the true precursor complex structures and only account for the main structural motifs present. The PDF data do not allow us to take into account interactions with solvent, cations, and base and their role in stabilizing the precursor complexes.

We also analyzed the precursor complexes appearing without adding base to the solutions. PDFs from these samples are shown in Figures S25−S27 and Tables S13−S15, showing that the precursor complexes display similar structures as those with base added. However, the XANES analysis, Figure S4, shows that it is only upon adding a base that the precursors start significantly reducing. Without base, the synthesis does not proceed to NPs. This can be expected assuming that the formation of alkoxide accounts for the formation of reducing agents for the reaction.[52] It can be expected that the different structures of the initial metal precursor complexes in solution at least partially account for the different NP formation pathway.[35]

**3.5. Formation of Transient Crystalline Structures and Effect of Base on Reaction Pathway.** *3.5.1. Presence of a*


https://doi.org/10.1021/jacs.2c10814
J. Am. Chem. Soc. XXXX, XXX, XXX−XXX

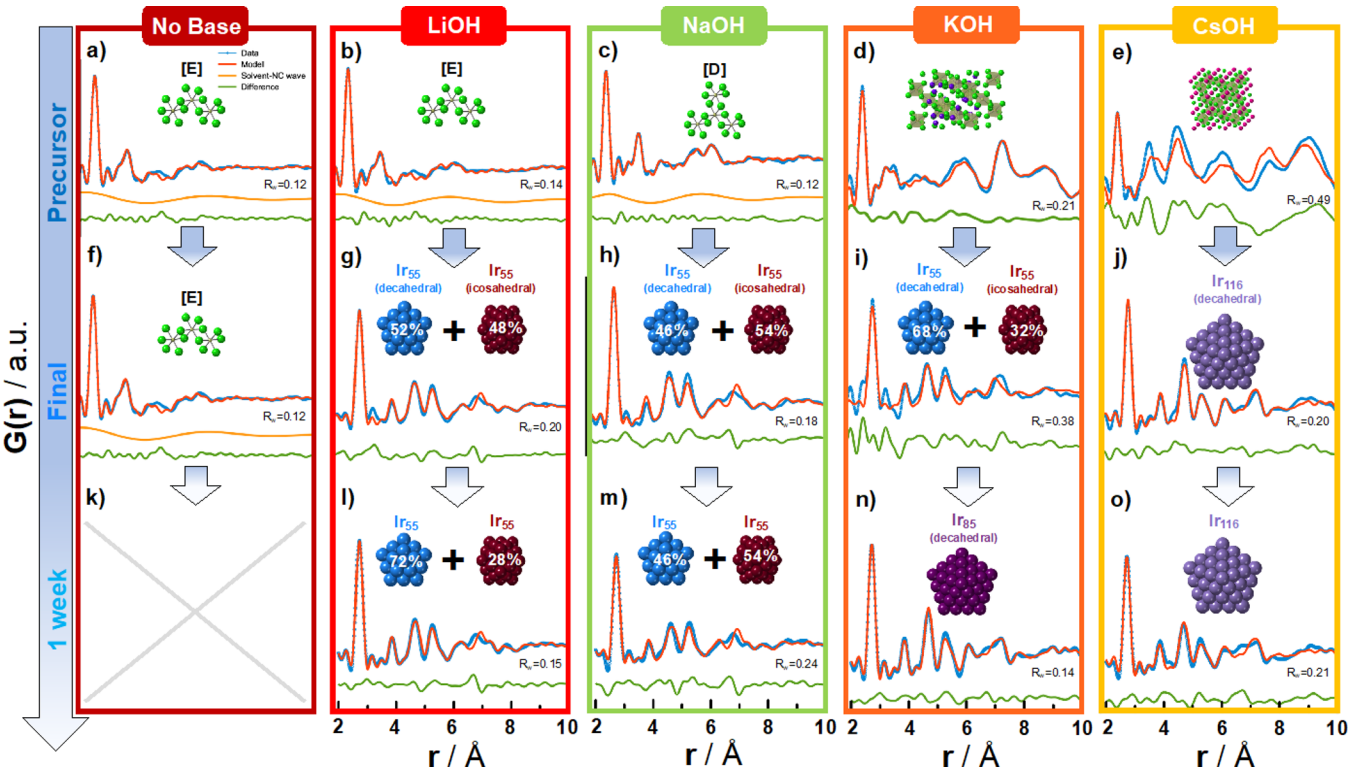


**Figure 5.** Modeling of (top, a−e) the precursor structures, (middle, f−j) the Ir NPs using $H_2IrCl_6$ as metal ion precursor after the *in situ* X-ray TS experiments, and (bottom, l−o) the Ir NPs formed after 1 week of synthesis when varying the base in the synthesis as indicated (a,f,k: No Base; b,g,l: LiOH; c,h,m: NaOH; d,i,n: KOH; e,j,o: CsOH). The models used in the refinement of each structure are presented above the refinement.

*Transient Crystalline Phase.* A remaining question is to clarify the nature and role of the transient crystalline species formed when $H_2IrCl_6$ is used, as well as the influence of the base on the reaction pathway. In Figure 1c,i, it was observed that a crystalline structure suddenly emerged 15 min into the experiment but disappeared as Ir NPs formed. This is clearly seen when examining the data in reciprocal space, $I(Q)$, in Figure S28a from the sudden appearance of intense Bragg peaks. However, as seen in Figure S28b, weaker and very broad peaks with the same peak position can already be identified in the scattering pattern from the precursor. Some of the structural features observed in the transient crystalline structure must thus already be present in the precursor structure. Several possible candidate structures were compared to the experimental data to attempt to identify the nature of the transient crystalline phase, see Figure S28. The crystalline phase could be a result of either a new Ir structure being formed or arising from ordering between separate units of the precursor complex structures. However, comparing the Bragg peaks to the reported structures of $IrO_2$, $Ir_6(CO)_{16}$, and $Ir(CO)_3Cl$ structure did not show any resemblance as observed in Figure S28c.[83−85] Oxides, hydroxides, and chlorides containing Ir or Na were also investigated due to the use of NaOH in the synthesis, including $Na_2IrCl_6$ and other Na-containing salts.[80,86,87] However, these structures could also not describe the Bragg peaks (Figure S28c).

To further clarify the role of NaOH in the formation of the crystalline phase, we also performed experiments using $Na_2IrCl_6$ as metal ion precursor with and without NaOH added. Figure S29a shows the PDF obtained when using $Na_2IrCl_6$ without NaOH where no crystalline phase was formed. However, the addition of NaOH to the reaction solution was found to immediately promote the formation of a crystalline structure as observed in Figure S29b. This crystalline phase remains throughout the reaction (Figure S29b,f); however, Ir NP formation is also observed, see Figure S29h. The formation of the crystalline phase thus appears to be dependent on alkaline conditions.

*3.5.2. Influence of Cations.* Motivated by this observation, and by the observation of a strong influence of cations in the surfactant-free synthesis of Pt NPs in alkaline MeOH,[88] we investigated the influence on cations on the reaction pathway. Using $H_2IrCl_6$ as the metal ion precursor, cations with increasing size were introduced, namely LiOH, KOH, and CsOH (where the cation size increases as $Li^+ < Na^+ < K^+ < Cs^+$). Additionally, an experiment was performed without any base present for comparison. Figure 4 shows the PDFs from the resulting data with increasing cation size. Each cation induces a significantly different formation pathway.

First, Figure 4a,f,k confirms that in the absence of a base, no Ir NPs form. By adding the smallest cation $Li^+$ using LiOH (Figure 4b,g,l), Ir NPs are found to form after ca. 15 min; however, unlike in the case of NaOH, no transient crystalline phase is observed. Instead, the Ir−Cl and Ir−Ir precursor structure PDF peaks are observed to slowly decrease, while the metallic Ir−Ir peak at 2.72 Å suddenly appears and rapidly increases. The metallic Ir−Ir peak intensity still increases as the experiment is terminated, and thus Ir NP formation continues beyond the time scale of the experiment. The use of KOH results in a crystalline precursor as evident by the appearance of peaks at high $r$ values. The structure can be identified as crystalline $K_3IrCl_6$ (Figure 5d, details of fit in Section 2.26 in SI), which is not soluble in MeOH. The PDFs (Figure 4i,n) show that metallic Ir−Ir peaks are found to emerge in the end of the experiment; however, the crystalline precursor phase remains due to its low solubility. We


https://doi.org/10.1021/jacs.2c10814
J. Am. Chem. Soc. XXXX, XXX, XXX−XXX

also note that toward the end of the experiment, "spotty" features were observed in the 2D detector images, showing the formation of large crystals, which is possibly related to the crystalline precursor. Finally, significant changes are observed when using CsOH as base. Just as KOH, the use of CsOH is found to lead to a crystalline $Cs_2IrCl_6$ precursor structure (Figure 5e). However, the structure clearly changes as Ir NPs begin to form, which is evident in the PDFs in Figure 4j. In Figure 4o, a rapid increase in the intensity of the Ir−Ir peak at 2.72 Å is observed. While the amount of precursor is reduced as seen by the decrease of Ir−Cl and Ir−Ir peak intensities from the precursor structure, Ir NPs rapidly form. This burst phenomenon could point toward autocatalytic surface growth as observed when using NaOH. The Ir NPs that emerge are, however, of a larger size than seen in experiments using other bases. This is especially evident in the PDFs, Figure 4e,j, where the final Ir structure emerging extends to higher $r$ values than observed with other bases. The particle size will be further addressed below. Some $Cs_2IrCl_6$ is preserved throughout the experiment, i.e., not all of the precursor has reacted at the end of the *in situ* experiment.

The rate of formation (i.e., the slope related to the increase in metallic Ir−Ir peak intensity) varied between the different cations used and did not show any clear trends. Although different speciation is induced when different bases are used, none of these systems illustrates the same transient crystalline structure formation as observed for NaOH/MeOH. Consequently, these results point toward the role of $Na^+$ and $MeO^-$ in the formation of the transient crystalline phase observed.

*3.5.3. Discussion.* Figure 4 summarizes the influence of different cations in the synthesis of Ir NPs from $H_2IrCl_6$. The experimental evidence provided here on the formation of a transient crystalline phase in the case where NaOH is used for the synthesis certainly opens a range of questions and important comments. First, the presence of this transient crystalline phase suggests a different formation pathway. Second, while the structure, nature, and the exact role (e.g., on-path or off-path intermediate) of this phase on the formation of Ir NPs remain challenging to fully address, we have, until now, only observed the transient crystalline phase when the initial precursor is expected to have octahedral $IrCl_6^{2-}$ geometry and when NaOH is used as base. This points toward the key role of the base and the geometry of the precursor for the formation of this transient structure. Although the data at this stage do not allow to identify the exact structure of the transient crystalline phase, it is likely to be mainly composed of Ir and Cl. This is in line with previous reports where $Au_nCl_y$[9] or $Pt_nCl_y$[77,89] was suggested to play a role in the formation of metallic NPs. It has even been suggested that species with the general formula $M_xCl_y$, generally with ill-defined stoichiometry and potentially partially reduced, are potential PNCs in the formation of metallic $M_n$ NPs.[35,76] Although the species observed here may be too stable to be kinetically effective considered PNCs, the different speciation noted for different starting precursor and base combinations suggests that the resulting PNCs will probably have different structures.

**3.6. Ir NP Structures Formed with Different Bases.** We now turn to the structure and size of the final Ir NPs formed using different bases. Since the presence of remaining precursor was observed within the time frame of the *in situ* experiment when using LiOH, KOH, and CsOH, a series of 1-week long experiments were also performed and the final product analyzed with PDF. The results are summarized in Figure 5. The refined values for all presented PDF refinements can be found in Tables S16−S20. Again, cluster mining was implemented to identify candidate structures for the Ir NPs formed. The results showed that the NPs obtained using LiOH can be described by the two-phase model with the Ino decahedral and icosahedral $Ir_{55}$ structures as also seen for NPs synthesized using NaOH. As seen in Figure 5g,l, this is the case for the NPs formed both at the end of the *in situ* experiment and after 1 week.

In the KOH synthesis, larger NPs were formed. While the presence of a high amount of unreacted, but continuously changing, precursor complicated the refinement of the data obtained in the *in situ* experiment (Figure 5i), the PDF from the product formed after the 1-week synthesis showed disappearance of the precursor, and Ir NPs that could be best described by a decahedral $Ir_{85}$ structure. For the Ir NPs formed in the presence of CsOH, it is retrieved from cluster mining that a large Ino decahedral $Ir_{116}$ structure is a possible candidate (Figure 5o) both in the *in situ* experiment and after 1 week. The fact that the larger particles that seem to appear are decahedral rather than icosahedral agrees well with previous considerations of metallic NP stability.[90,91] The general trend thus shows that the larger the cation, the larger NPs formed in the synthesis, which thereby provides a fine size control missing to date for the surfactant-free Ir NPs.[59]

## 4. CONCLUSIONS

Using *in situ* X-ray TS and PDF analysis, detailed structural insights into the formation of Ir NPs are reported. A simple, low temperature, surfactant-free synthesis in alkaline MeOH was used. By studying the influence of different precursors ($IrCl_3$, $IrCl_4$, $H_2IrCl_6$, and $Na_2IrCl_6$) and bases (LiOH, NaOH, KOH, and CsOH), several substantial findings are reported regarding the NP formation process. Despite not using surfactants, small size Ir NPs (<2 nm) are readily obtained even at high precursor concentration of 100 mM. The NPs are expected to be stabilized by adsorbed species such as $CO_{ad}$ and electrostatic interactions. Ir NPs can furthermore form at relatively low temperature, which shows promising scalability of the method to develop for instance highly active catalysts.[42,46,60]

Our results show that both the precursor salt, as well as the nature of the base added, have an influence on the reaction pathway and the NPs formed. The first species formed under alkaline conditions in MeOH can be described as $Ir_xCl_y$ species such as $Ir_4Cl_{18}^{n-}$ to $Ir_6Cl_{26}^{n-}$. The resulting NPs show non-*fcc* icosahedral and decahedral structures. As the cation size increase, the size of the final NPs increases when $H_2IrCl_6$ is used as metal ion precursor. The average NP size can be controlled from $Ir_{\sim 55}$ to $Ir_{\sim 86}$ or $Ir_{\sim 116}$.

The reaction pathway is highly dependent on the reaction conditions. Ir NPs form from clusters of $Ir_nCl_y$ as it has previously been seen also for Au and Pt. However, even seemingly small differences in the synthesis procedure, such as the change from $IrCl_3$ or $IrCl_4$ to $H_2IrCl_6$, change the reaction route. A transient crystalline structure forms in the case of $H_2IrCl_6$, but only when used in the presence of NaOH. These results stress the probably overlooked effect of cations in colloidal syntheses.

The results presented open a range of questions and opportunities. First, the sudden formation and disappearance of a crystalline phase observed before Ir NPs form seem to lead to a burst-growth-like formation of Ir NPs.[45] While the exact nature of this transient structure is still unclear, $M_nCl_y$ intermediate structures such as $Pt_nCl_y$ were previously


https://doi.org/10.1021/jacs.2c10814
J. Am. Chem. Soc. XXXX, XXX, XXX−XXX

reported.[77] Clarifying if $M_xCl_y$ transition metal structures are always observed, when such burst-growth-like behavior is at stake, may provide new insights. Second, with recent exciting results, methods development such as mechanism-enabled population balance modeling (ME-PBM)[22] and refinement of kinetics models,[22] we anticipate that the insights provided here will help to further improve our understanding of the mechanism(s) of formation of Ir NPs, for instance by ultimately making the predictions from ME-PBM even more powerful and accurate.

While this work provides a detailed study of the strong influence of seemingly simple parameters in Ir NP synthesis, further work is certainly needed, e.g., to understand the interaction between the cations and $Ir_nCl_y$ clusters and provide a more complete picture of the NP formation. Nevertheless, the results highlight the importance of considering the chemical species present and formed when attempting to understand and control further NP formation.

## ■ ASSOCIATED CONTENT

### Supporting Information

The Supporting Information is available free of charge at https://pubs.acs.org/doi/10.1021/jacs.2c10814.

Details on experimental data, models used and fits performed for PDF analysis, Pearson correlation and DFT calculation together with reproduced data, TEM, XAS, SAXS, GCMS, and FTIR characterization (PDF)

## ■ AUTHOR INFORMATION


### Corresponding Authors

**Jonathan Quinson** − *Department of Chemistry, University of Copenhagen, 2100 Copenhagen Ø, Denmark; Department of Biochemical and Chemical Engineering, Aarhus University, 8200 Aarhus N, Denmark;* orcid.org/0000-0002-9374-9330; Email: jquinson@bce.au.dk

**Kirsten M. Ø. Jensen** − *Department of Chemistry, University of Copenhagen, 2100 Copenhagen Ø, Denmark;* orcid.org/0000-0003-0291-217X; Email: kirsten@chem.ku.dk

### Authors

**Jette K. Mathiesen** − *Department of Chemistry, University of Copenhagen, 2100 Copenhagen Ø, Denmark; Department of Physics, Technical University of Denmark, 2800 Kgs. Lyngby, Denmark*

**Sonja Blaseio** − *Institute of Technical Chemistry, Technische Universität Braunschweig, 38106 Braunschweig, Germany;* orcid.org/0000-0001-5410-994X

**Emil T. S. Kjær** − *Department of Chemistry, University of Copenhagen, 2100 Copenhagen Ø, Denmark*

**Alexandra Dworzak** − *Institute of Technical Chemistry, Technische Universität Braunschweig, 38106 Braunschweig, Germany;* orcid.org/0000-0002-8689-9517

**Susan R. Cooper** − *Department of Chemistry, University of Copenhagen, 2100 Copenhagen Ø, Denmark*

**Jack K. Pedersen** − *Department of Chemistry, University of Copenhagen, 2100 Copenhagen Ø, Denmark;* orcid.org/0000-0002-5601-5450

**Baiyu Wang** − *Department of Chemistry, University of Copenhagen, 2100 Copenhagen Ø, Denmark*

**Francesco Bizzotto** − *Department of Chemistry, Biochemistry, and Pharmaceutical Sciences, University of Bern, CH-3012 Bern, Switzerland*

**Johanna Schröder** − *Department of Chemistry, Biochemistry, and Pharmaceutical Sciences, University of Bern, CH-3012 Bern, Switzerland;* orcid.org/0000-0001-5461-4751

**Tiffany L. Kinnibrugh** − *X-ray Science Division, Advanced Photon Source, Argonne National Laboratory, Lemont, Illinois 60439, United States*

**Søren B. Simonsen** − *Department of Energy Conversion and Storage, Technical University of Denmark, 2800 Kgs. Lyngby, Denmark;* orcid.org/0000-0001-7172-1225

**Luise Theil Kuhn** − *Department of Energy Conversion and Storage, Technical University of Denmark, 2800 Kgs. Lyngby, Denmark*

**Jacob J. K. Kirkensgaard** − *Department of Food Science, University of Copenhagen, 1958 Frederiksberg C, Denmark; Niels-Bohr-Institute, University of Copenhagen, 2100 Copenhagen Ø, Denmark;* orcid.org/0000-0001-6265-0314

**Jan Rossmeisl** − *Department of Chemistry, University of Copenhagen, 2100 Copenhagen Ø, Denmark;* orcid.org/0000-0001-7749-6567

**Mehtap Oezaslan** − *Institute of Technical Chemistry, Technische Universität Braunschweig, 38106 Braunschweig, Germany;* orcid.org/0000-0001-8545-7576

**Matthias Arenz** − *Department of Chemistry, Biochemistry, and Pharmaceutical Sciences, University of Bern, CH-3012 Bern, Switzerland;* orcid.org/0000-0001-9765-4315

Complete contact information is available at: https://pubs.acs.org/10.1021/jacs.2c10814


### Author Contributions

¶J.K.M. and J.Q. contributed equally to this study.

### Author Contributions

All authors have given approval to the final version of the manuscript.


### Funding

We are grateful for funding from the Villum Foundation through a Villum Young Investigator Grant (VKR00015416). Funding from the Danish Ministry of Higher Education and Science through the SMART Lighthouse is gratefully acknowledged. We acknowledge support from the Danish National Research Foundation Center for High Entropy Alloy Catalysis (DNRF 149). M.A. received funding from the Swiss National Science Foundation (SNSF) via the project no. 200021 184742. The Danish Research Council is acknowledged for covering travel expenses in relation to the synchrotron experiment (DanScatt).


### Notes

The authors declare no competing financial interest.

## ■ ACKNOWLEDGMENTS


The authors would like to acknowledge the staff of beamline 11-ID-Bat Argonne National Laboratory (APS) for experimental assistance, in particular, O. J. Borkiewicz and C. Leighanne. Use of the Advanced Photon Source, an Office of Science User Facility operated for the U.S. Department of Energy (DOE) Office of Science by Argonne National Laboratory, was supported by the U.S. DOE under contract no. DE-AC02-06CH11357 for the project GUP-65450 and GUP-73929. We gratefully thank Valerie Briois and Laurent Barthe for the technical support at the ROCK beamline, SOLEIL, France (Proposal ID 20190317). The work at the ROCK beamline was supported by a public grant overseen by the French National Research Agency (ANR) as part of the "Investissements

d'Avenir" program (reference, ANR10-EQPX45). M.O. thanks the Ministerium für Bildung und Forschung (BMBF, ECatPEMFC, FKZ 03SF0539). We would like to thank Dr. Christopher Whitehead for fruitful discussion on kinetic modeling.

## REFERENCES

(1) Strach, M.; Mantella, V.; Pankhurst, J. R.; Iyengar, P.; Loiudice, A.; Das, S.; Corminboeuf, C.; van Beek, W.; Buonsanti, R. Insights into Reaction Intermediates to Predict Synthetic Pathways for Shape-Controlled Metal Nanocrystals. *J. Am. Chem. Soc.* **2019**, *141*, 16312−16322.

(2) Aalling-Frederiksen, O.; Juelsholt, M.; Anker, A. S.; Jensen, K. M. Formation and growth mechanism for niobium oxide nanoparticles: atomistic insight from in situ X-ray total scattering. *Nanoscale* **2021**, *13*, 8087−8097.

(3) Jensen, K. M. Ø.; Andersen, H. L.; Tyrsted, C.; Bøjesen, E. D.; Dippel, A.-C.; Lock, N.; Billinge, S. J. L.; Iversen, B. B.; Christensen, M. Mechanisms for Iron Oxide Formation under Hydrothermal Conditions: An in Situ Total Scattering Study. *ACS Nano* **2014**, *8*, 10704−10714.

(4) Jensen, K. M. Ø.; Christensen, M.; Juhas, P.; Tyrsted, C.; Bøjesen, E. D.; Lock, N.; Billinge, S. J.; Iversen, B. B. Revealing the mechanisms behind $SnO_2$ nanoparticle formation and growth during hydrothermal synthesis: an in situ total scattering study. *J. Am. Chem. Soc.* **2012**, *134*, 6785−6792.

(5) Whitehead, C. B.; Ozkar, S.; Finke, R. G. LaMer's 1950 model of particle formation: a review and critical analysis of its classical nucleation and fluctuation theory basis, of competing models and mechanisms for phase-changes and particle formation, and then of its application to silver halide, semiconductor, metal, and metal-oxide nanoparticles. *Mater. Adv.* **2021**, *2*, 186−235.

(6) Cheong, S.; Watt, J.; Ingham, B.; Toney, M. F.; Tilley, R. D. In Situ and Ex Situ Studies of Platinum Nanocrystals: Growth and Evolution in Solution. *J. Am. Chem. Soc.* **2009**, *131*, 14590−14595.

(7) Wuithschick, M.; Birnbaum, A.; Witte, S.; Sztucki, M.; Vainio, U.; Pinna, N.; Rademann, K.; Emmerling, F.; Kraehnert, R.; Polte, J. Turkevich in New Robes: Key Questions Answered for the Most Common Gold Nanoparticle Synthesis. *ACS Nano* **2015**, *9*, 7052−7071.

(8) Chen, S. M.; Yang, Q. Y.; Wang, H. H.; Zhang, S.; Li, J.; Wang, Y.; Chu, W. S.; Ye, Q.; Song, L. Initial Reaction Mechanism of Platinum Nanoparticle in Methanol-Water System and the Anomalous Catalytic Effect of Water. *Nano Lett.* **2015**, *15*, 5961−5968.

(9) Yao, T.; Sun, Z. H.; Li, Y. Y.; Pan, Z. Y.; Wei, H.; Xie, Y.; Nomura, M.; Niwa, Y.; Yan, W. S.; Wu, Z. Y.; et al. Insights into Initial Kinetic Nucleation of Gold Nanocrystals. *J. Am. Chem. Soc.* **2010**, *132*, 7696−7701.

(10) Becker, J.; Bremholm, M.; Tyrsted, C.; Pauw, B.; Jensen, K. M. Ø.; Eltzholt, J.; Christensen, M.; Iversen, B. B. Experimental setup for in situ X-ray SAXS/WAXS/PDF studies of the formation and growth of nanoparticles in near- and supercritical fluids. *J. Appl. Crystallogr.* **2010**, *43*, 729−736.

(11) Whitehead, C. B.; Finke, R. G. Particle formation mechanisms supported by in situ synchrotron XAFS and SAXS studies: a review of metal, metal-oxide, semiconductor and selected other nanoparticle formation reactions. *Mater. Adv.* **2021**, *2*, 6532−6568.

(12) Uzun, A.; Gates, B. C. Real-Time Characterization of Formation and Breakup of Iridium Clusters in Highly Dealuminated Zeolite Y. *Angew. Chem., Int. Ed.* **2008**, *47*, 9245−9248.

(13) Cooper, C.; Dooley, K. M.; Fierro-Gonzalez, J. C.; Guzman, J.; Jentoft, R.; Lamb, H. H.; Ogino, I.; Runnebaum, R. C.; Sapre, A.; Uzun, A. Bruce Gates: A Career in Catalysis. *ACS Catal.* **2020**, *10*, 11912−11935.

(14) Cargnello, M. Colloidal Nanocrystals as Building Blocks for Well-Defined Heterogeneous Catalysts. *Chem. Mater.* **2019**, *31*, 576−596.

(15) Saldanha, P. L.; Lesnyak, V.; Manna, L. Large scale syntheses of colloidal nanomaterials. *Nano Today* **2017**, *12*, 46−63.

(16) Thanh, N. T. K.; Maclean, N.; Mahiddine, S. Mechanisms of Nucleation and Growth of Nanoparticles in Solution. *Chem. Rev.* **2014**, *114*, 7610−7630.

(17) Quinson, J.; Jensen, K. M. Ø. From platinum atoms in molecules to colloidal nanoparticles: a review on reduction, nucleation and growth mechanisms. *Adv. Colloid Interface Sci.* **2020**, *286*, No. 102300.

(18) Quinson, J.; Neumann, S.; Kacenauskaite, L.; Bucher, J.; Kirkensgaard, J. J. K.; Simonsen, S. B.; Kuhn, L. T.; Zana, A.; Vosch, T.; Oezaslan, M.; et al. Solvent-Dependent Growth and Stabilization Mechanisms of Surfactant-Free Colloidal Pt Nanoparticles. *Chem. − Eur. J.* **2020**, *26*, 9012−9023.

(19) Lettenmeier, P.; Majchel, J.; Wang, L.; Saveleva, V. A.; Zafeiratos, S.; Savinova, E. R.; Gallet, J. J.; Bournel, F.; Gago, A. S.; Friedrich, K. A. Highly active nano-sized iridium catalysts: synthesis and operando spectroscopy in a proton exchange membrane electrolyzer. *Chem. Sci.* **2018**, *9*, 3570−3579.

(20) Rodrigues, T. S.; Zhao, M.; Yang, T. H.; Gilroy, K. D.; da Silva, A. G. M.; Camargo, P. H. C.; Xia, Y. N. Synthesis of Colloidal Metal Nanocrystals: A Comprehensive Review on the Reductants. *Chem. − Eur. J.* **2018**, *24*, 16944−16963.

(21) Finney, E. E.; Finke, R. G. Nanocluster nucleation and growth kinetic and mechanistic studies: A review emphasizing transition-metal nanoclusters. *J. Colloid Interface Sci.* **2008**, *317*, 351−374.

(22) Handwerk, D. R.; Shipman, P. D.; Whitehead, C. B.; Ozkar, S.; Finke, R. G. Mechanism-Enabled Population Balance Modeling of Particle Formation en Route to Particle Average Size and Size Distribution Understanding and Control. *J. Am. Chem. Soc.* **2019**, *141*, 15827−15839.

(23) Quinson, J. Iridium and $IrO_x$ nanoparticles: an overview and review of syntheses and applications. *Adv. Colloid Interface Sci.* **2022**, *303*, No. 102643.

(24) Ozkar, S.; Finke, R. G. Nanoparticle Nucleation Is Termolecular in Metal and Involves Hydrogen: Evidence for a Kinetically Effective Nucleus of Three $\{Ir_3H_{2x}P_2W_{15}Nb_3O_{62}\}^{6-}$ in $Ir(0)_n$ Nanoparticle Formation From $[(1,5\text{-COD})Ir^{I}P_2W_{15}Nb_3O_{62}]^{8-}$ Plus Dihydrogen. *J. Am. Chem. Soc.* **2017**, *139*, 5444−5457.

(25) Ali, I.; AlGhamdi, K.; Al-Wadaani, F. T. Advances in iridium nano catalyst preparation, characterization and applications. *J. Mol. Liq.* **2019**, *280*, 274−284.

(26) Fonseca, G. S.; Machado, G.; Teixeira, S. R.; Fecher, G. H.; Morais, J.; Alves, M. C. M.; Dupont, J. Synthesis and characterization of catalytic iridium nanoparticles in imidazolium ionic liquids. *J. Colloid Interface Sci.* **2006**, *301*, 193−204.

(27) Colby, D. A.; Bergman, R. G.; Ellman, J. A. Stereoselective alkylation of alpha,beta-unsaturated imines via C-H bond activation. *J. Am. Chem. Soc.* **2006**, *128*, 5604−5605.

(28) Cui, M. L.; Chen, Y. S.; Xie, Q. F.; Yang, D. P.; Han, M. Y. Synthesis, properties and applications of noble metal iridium nanomaterials. *Coord. Chem. Rev.* **2019**, *387*, 450−462.

(29) Brown, A. L.; Winter, H.; Goforth, A. M.; Sahay, G.; Sun, C. Facile Synthesis of Ligand-Free Iridium Nanoparticles and Their In Vitro Biocompatibility. *Nanoscale Res. Lett.* **2018**, *13*, 208.

(30) Meiring, J. J.; Borm, P. J. A.; Bagate, K.; Semmler, M.; Seitz, J.; Takenaka, S.; Kreyling, W. G. The influence of hydrogen peroxide and histamine on lung permeability and translocation of iridium nanoparticles in the isolated perfused rat lung. *Part. Fibre Toxicol.* **2005**, *2*, 3.

(31) Wang, C.; Lan, F. F.; He, Z. F.; Xie, X. F.; Zhao, Y. H.; Hou, H.; Guo, L.; Murugadoss, V.; Liu, H.; Shao, Q.; et al. Iridium-Based Catalysts for Solid Polymer Electrolyte Electrocatalytic Water Splitting. *ChemSusChem* **2019**, *12*, 1576−1590.

(32) Watzky, M. A.; Finke, R. G. Nanocluster size-control and "magic number" investigations, experimental tests of the "living-metal polymer" concept and of mechanism-based size-control predictions leading to the syntheses of iridium(0) nanoclusters centering about four sequential magic numbers. *Chem. Mater.* **1997**, *9*, 3083−3095.

(33) Watzky, M. A.; Finke, R. G. Transition metal nanocluster formation kinetic and mechanistic studies. A new mechanism when hydrogen is the reductant: Slow, continuous nucleation and fast



https://doi.org/10.1021/jacs.2c10814
J. Am. Chem. Soc. XXXX, XXX, XXX−XXX

autocatalytic surface growth. *J. Am. Chem. Soc.* **1997**, *119*, 10382−10400.
(34) Whitehead, C. B.; Finke, R. G. Nucleation Kinetics and Molecular Mechanism in Transition-Metal Nanoparticle Formation: The Intriguing, Informative Case of a Bimetallic Precursor, $\{[(1,5\text{-COD})Ir^{I}\cdot HPO_4]_2\}^{2-}$. *Chem. Mater.* **2019**, *31*, 2848−2862.
(35) Gebauer, D.; Kellermeier, M.; Gale, J. D.; Bergström, L.; Cölfen, H. Pre-nucleation clusters as solute precursors in crystallisation. *Chem. Soc. Rev.* **2014**, *43*, 2348−2371.
(36) Bojesen, E. D.; Iversen, B. B. The chemistry of nucleation. *CrystEngComm* **2016**, *18*, 8332−8353.
(37) Loh, N. D.; Sen, S.; Bosman, M.; Tan, S. F.; Zhong, J.; Nijhuis, C. A.; Král, P.; Matsudaira, P.; Mirsaidov, U. Multistep nucleation of nanocrystals in aqueous solution. *Nat. Chem.* **2017**, *9*, 77.
(38) Smeets, P. J. M.; Finney, A. R.; Habraken, W. J. E. M.; Nudelman, F.; Friedrich, H.; Laven, J.; De Yoreo, J. J.; Rodger, P. M.; Sommerdijk, N. A. J. M. A classical view on nonclassical nucleation. *Proc. Natl. Acad. Sci. U. S. A.* **2017**, *114*, No. E7882.
(39) Stowell, C. A.; Korgel, B. A. Iridium nanocrystal synthesis and surface coating-dependent catalytic activity. *Nano Lett.* **2005**, *5*, 1203−1207.
(40) Arminio-Ravelo, J. A.; Quinson, J.; Pedersen, M. A.; Kirkensgaard, J. J. K.; Arenz, M.; Escudero-Escribano, M. Synthesis of Iridium Nanocatalysts for Water Oxidation in Acid: Effect of the Surfactant. *ChemCatChem* **2020**, *12*, 1282−1287.
(41) Lin, Y.; Finke, R. G. Novel polyoxoanion-stabilized and $Bu_4N^+$-stabilized, isolable, and redissolable 20-30 ångstrom $Ir_{300\text{-}900}$ nanoclusters: The kinetically controlld synthesis, characterization and mechanism of formation of organic solvent-soluble, reproducible size, and reproducible catalytic activity metal nanoclusters. *J. Am. Chem. Soc.* **1994**, *116*, 8335−8353.
(42) Quinson, J.; Neumann, S.; Wannmacher, T.; Kacenauskaite, L.; Inaba, M.; Bucher, J.; Bizzotto, F.; Simonsen, S. B.; Kuhn, L. T.; Bujak, D.; et al. Colloids for Catalysts: A Concept for the Preparation of Superior Catalysts of Industrial Relevance. *Angew. Chem., Int. Ed.* **2018**, *57*, 12338−12341.
(43) Mathiesen, J. K.; Cooper, S. R.; Anker, A. S.; Kinnibrugh, T. L.; Jensen, K. M. Ø.; Quinson, J. Simple Setup Miniaturization with Multiple Benefits for Green Chemistry in Nanoparticle Synthesis. *ACS Omega* **2022**, *7*, 4714−4721.
(44) Christiansen, T. L.; Cooper, S. R.; Jensen, K. M. Ø. There's no place like real-space: elucidating size-dependent atomic structure of nanomaterials using pair distribution function analysis. *Nanoscale Adv.* **2020**, *2*, 2234−2254.
(45) Whitehead, C. B.; Watzky, M. A.; Finke, R. G. "Burst Nucleation" vs Autocatalytic, "Burst" Growth in Near-Monodisperse Particle-Formation Reactions. *J. Phys. Chem. C* **2020**, *124*, 24543−24554.
(46) Bizzotto, F.; Quinson, J.; Zana, A.; Kirkensaard, J. J. K.; Dworzak, A.; Oezaslan, M.; Arenz, M. Ir nanoparticles with ultrahigh dispersion as oxygen evolution reaction (OER) catalysts: synthesis and activity benchmarking. *Catal. Sci. Technol.* **2019**, *9*, 6345−6356.
(47) Hammersley, A. P.; Svensson, S. O.; Hanfland, M.; Fitch, A. N.; Hausermann, D. Two-dimensional detector software: From real detector to idealised image or two-theta scan. *High Pressure Res.* **1996**, *14*, 235−248.
(48) Hammersley, A. P. FIT2D: a multi-purpose data reduction, analysis and visualization program. *J. Appl. Crystallogr.* **2016**, *49*, 646−652.
(49) Toby, B. H.; Von Dreele, R. B. GSAS-II: the genesis of a modern open-source all purpose crystallography software package. *J. Appl. Crystallogr.* **2013**, *46*, 544−549.
(50) Juhas, P.; Davis, T.; Farrow, C. L.; Billinge, S. J. L. PDFgetX3: a rapid and highly automatable program for processing powder diffraction data into total scattering pair distribution functions. *J. Appl. Crystallogr.* **2013**, *46*, 560−566.
(51) Juhas, P.; Farrow, C. L.; Yang, X.; Knox, K. R.; Billinge, S. J. L. Complex modeling: a strategy and software program for combining multiple information sources to solve ill posed structure and nanostructure inverse problems. *Acta Crystallogr. A* **2015**, *71*, 562−568.
(52) Gomes, J. F.; Garcia, A. C.; Ferreira, E. B.; Pires, C.; Oliveira, V. L.; Tremiliosi-Filho, G.; Gasparotto, L. H. S. New insights into the formation mechanism of Ag, Au and AgAu nanoparticles in aqueous alkaline media: alkoxides from alcohols, aldehydes and ketones as universal reducing agents. *Phys. Chem. Chem. Phys.* **2015**, *17*, 21683−21693.
(53) Pabsch, D.; Figiel, P.; Sadowski, G.; Held, C. Solubility of Electrolytes in Organic Solvents: Solvent-Specific Effects and Ion-Specific Effects. *J. Chem. Eng. Data* **2022**, *67*, 2706−2718.
(54) Halpern, J. Some aspects of chemical dynamics in solution. *J. Chem. Educ.* **1968**, *45*, 372.
(55) Meisel, A.; Leonhardt, G. Die Kristallstruktur von $\beta$-Iridium (III)-Chlorid. *Z. Anorg. Allg. Chem.* **1965**, *339*, 57−66.
(56) Hull, A. W. X-ray crystal analysis of thirteen common metals. *Phys. Rev.* **1921**, *17*, 571.
(57) Whitehead, C. B.; Handwerk, D. R.; Shipman, P. D.; Li, Y. Y.; Frenkel, A. I.; Ingham, B.; Kirby, N. M.; Finke, R. G. Nanoparticle Formation Kinetics, Mechanisms, and Accurate Rate Constants: Examination of a Second-Generation $Ir(0)_n$ Particle Formation System by Five Monitoring Methods Plus Initial Mechanism-Enabled Population Balance Modeling. *J. Phys. Chem. C* **2021**, *125*, 13449−13476.
(58) Besson, C.; Finney, E. E.; Finke, R. G. Nanocluster nucleation, growth, and then agglomeration kinetic and mechanistic studies: A more general, four-step mechanism involving double autocatalysis. *Chem. Mater.* **2005**, *17*, 4925−4938.
(59) Quinson, J.; Kacenauskaite, L.; Schroder, J.; Simonsen, S. B.; Kuhn, L. T.; Vosch, T.; Arenz, M. UV-induced syntheses of surfactant-free precious metal nanoparticles in alkaline methanol and ethanol. *Nanoscale Adv.* **2020**, *2*, 2288−2292.
(60) Bizzotto, F.; Quinson, J.; Schröder, J.; Zana, A.; Arenz, M. Surfactant-free colloidal strategies for highly dispersed and active supported $IrO_2$ catalysts: Synthesis and performance evaluation for the oxygen evolution reaction. *J. Catal.* **2021**, *401*, 54−62.
(61) Bonet, F.; Delmas, V.; Grugeon, S.; Urbina, R. H.; Silvert, P. Y.; Tekaia-Elhsissen, K. Synthesis of monodisperse Au, Pt, Pd, Ru and Ir nanoparticles in ethylene glycol. *Nanostruct. Mater.* **1999**, *11*, 1277−1284.
(62) Ino, S.; Ogawa, S. Multiply twinned particles at earlier stages of gold film formation on alkalihalide crystals. *J. Phys. Soc. Jpn.* **1967**, *22*, 1365−1374.
(63) Marks, L.; Smith, D. J. High resolution studies of small particles of gold and silver: I. Multiply-twinned particles. *J. Cryst. Growth* **1981**, *54*, 425−432.
(64) Marks, L. Surface structure and energetics of multiply twinned particles. *Philos. Mag. A* **1984**, *49*, 81−93.
(65) Marks, L. Experimental studies of small particle structures. *Rep. Prog. Phys.* **1994**, *57*, 603.
(66) Schmid, G. Cluster and Colloids - bridges bewteen molecular and condensed material. *Endeavour* **1990**, *14*, 172−178.
(67) Jensen, K. M. Ø.; Juhas, P.; Tofanelli, M. A.; Heinecke, C. L.; Vaughan, G.; Ackerson, C. J.; Billinge, S. J. L. Polymorphism in magic-sized $Au_{144}(SR)_{60}$ clusters. *Nat. Commun.* **2016**, *7*, 11859.
(68) Lim, B.; Wang, J. G.; Camargo, P. H. C.; Cobley, C. M.; Kim, M. J.; Xia, Y. N. Twin-Induced Growth of Palladium-Platinum Alloy Nanocrystals. *Angew. Chem., Int. Ed.* **2009**, *48*, 6304−6308.
(69) Banerjee, S.; Liu, C. H.; Jensen, K. M. Ø.; Juhas, P.; Lee, J. D.; Tofanelli, M.; Ackerson, C. J.; Murray, C. B.; Billinge, S. J. L. Cluster-mining: an approach for determining core structures of metallic nanoparticles from atomic pair distribution function data. *Acta Crystallogr. A* **2020**, *76*, 24−31.
(70) Larsen, A. H.; Mortensen, J. J.; Blomqvist, J.; Castelli, I. E.; Christensen, R.; Dułak, M.; Friis, J.; Groves, M. N.; Hammer, B.; Hargus, C. The atomic simulation environment—a Python library for working with atoms. *J. Phys.: Condens. Matter* **2017**, *29*, 273002.
(71) Bayram, E.; Lu, J.; Aydin, C.; Browning, N. D.; Ozkar, S.; Finney, E.; Gates, B. C.; Finke, R. G. Agglomerative Sintering of an Atomically Dispersed Ir-1/Zeolite Y Catalyst: Compelling Evidence Against


https://doi.org/10.1021/jacs.2c10814
J. Am. Chem. Soc. XXXX, XXX, XXX−XXX

Ostwald Ripening but for Bimolecular and Autocatalytic Agglomeration Catalyst Sintering Steps. *ACS Catal.* **2015**, *5*, 3514−3527.
(72) Crooks, A. B.; Yih, K. H.; Li, L.; Yang, J. C.; Ozkar, S.; Finke, R. G. Unintuitive Inverse Dependence of the Apparent Turnover Frequency on Precatalyst Concentration: A Quantitative Explanation in the Case of Ziegler-Type Nanoparticle Catalysts Made from $[(1,5\text{-COD})Ir(\mu\text{-}O_2C_8H_{15})]_2$ and $AlEt_3$. *ACS Catal.* **2015**, *5*, 3342−3353.
(73) Pawluk, T.; Hirata, Y.; Wang, L. C. Studies of iridium nanoparticles using density functional theory calculations. *J. Phys. Chem. B* **2005**, *109*, 20817−20823.
(74) Kjær, E. T. S.; Aalling-Frederiksen, O.; Yang, L.; Thomas, N. K.; Billinge, S. J. L.; Jensen, K. M. Ø. In Situ Studies of the Formation of Tungsten and Niobium Oxide Nanoparticles: Towards Automated Analysis of Reaction Pathways from PDF Analysis using the Pearson Correlation Coefficient. *Chem. Methods* **2022**, *2*, No. e202200034.
(75) Mozaffari, S.; Li, W. H.; Dixit, M.; Seifert, S.; Lee, B.; Kovarik, L.; Mpourmpakis, G.; Karim, A. M. The role of nanoparticle size and ligand coverage in size focusing of colloidal metal nanoparticles. *Nanoscale Adv.* **2019**, *1*, 4052−4066.
(76) Ramamoorthy, R. K.; Yildirim, E.; Barba, E.; Roblin, P.; Vargas, J. A.; Lacroix, L. M.; Rodriguez-Ruiz, I.; Decorse, P.; Petkov, V.; Teychene, S.; et al. The role of pre-nucleation clusters in the crystallization of gold nanoparticles. *Nanoscale* **2020**, *12*, 16173−16188.
(77) Mathiesen, J. K.; Quinson, J.; Dworzak, A.; Vosch, T.; Juelsholt, M.; Kjaer, E. T. S.; Schroder, J.; Kirkensgaard, J. J. K.; Oezaslan, M.; Arenz, M.; et al. Insights from In Situ Studies on the Early Stages of Platinum Nanoparticle Formation. *J. Phys. Chem. Lett.* **2021**, *12*, 3224−3231.
(78) Brodersen, K.; Moers, F.; Schnering, H. Zur Struktur des Iridium (III)-und des Ruthenium (III)-chlorids. *Naturwissenschaften* **1965**, *52*, 205−206.
(79) Coll, R. K.; Fergusson, S. E.; Penfold, B. R.; Rankin, D. A.; Robinson, W. T. The preparative and structural chemistries of hexahalogeno and trichlorostannato complexes of iridium. *Inorg. Chim. Acta* **1990**, *177*, 107−114.
(80) Bao, S.-S.; Wang, D.; Huang, X.-D.; Etter, M.; Cai, Z.-S.; Wan, X.; Dinnebier, R. E.; Zheng, L.-M. $Na_2Ir^{IV}Cl_6$: Spin−Orbital-Induced Semiconductor Showing Hydration-Dependent Structural and Magnetic Variations. *Inorg. Chem.* **2018**, *57*, 13252−13258.
(81) Zobel, M.; Neder, R. B.; Kimber, S. A. J. Universal solvent restructuring induced by colloidal nanoparticles. *Science* **2015**, *347*, 292−294.
(82) Anker, A. S.; Christiansen, T. L.; Weber, M.; Schmiele, M.; Brok, E.; Kjaer, E. T. S.; Juhas, P.; Thomas, R.; Mehring, M.; Jensen, K. M. Ø. Structural Changes during the Growth of Atomically Precise Metal Oxido Nanoclusters from Combined Pair Distribution Function and Small-Angle X-ray Scattering Analysis. *Angew. Chem., Int. Ed.* **2021**, *60*, 20407−20416.
(83) Reis, A., Jr.; Hagley, V.; Peterson, S. Stabilization of one-dimensional conducting materials by carbonyl ligands. Crystal and molecular structure of tricarbonylchloroiridium. *J. Am. Chem. Soc.* **1977**, *99*, 4184−4186.
(84) Bolzan, A. A.; Fong, C.; Kennedy, B. J.; Howard, C. J. Structural studies of rutile-type metal dioxides. *Acta Crystallogr. B* **1997**, *53*, 373−380.
(85) Garlaschelli, L.; Martinengo, S.; Bellon, P. L.; Demartin, F.; Manassero, M.; Chiang, M. Y.; Wei, C.-Y.; Bau, R. Structures of two isomers of hexairidium hexadecacarbonyl. *J. Am. Chem. Soc.* **1984**, *106*, 6664−6667.
(86) Fontana, P.; Schefer, J.; Pettit, D. Characterization of sodium chloride crystals grown in microgravity. *J. Cryst. Growth* **2011**, *324*, 207−211.
(87) Sowa, H. The high-pressure behavior of $NaClO_3$. *J. Solid State Chem.* **1995**, *118*, 378−382.
(88) Quinson, J.; Bucher, J.; Simonsen, S. B.; Kuhn, L. T.; Kunz, S.; Arenz, M. Monovalent Alkali Cations: Simple and Eco-Friendly Stabilizers for Surfactant-Free Precious Metal Nanoparticle Colloids. *ACS Sustainable Chem. Eng.* **2019**, *7*, 13680−13686.
(89) Yao, T.; Liu, S. J.; Sun, Z. H.; Li, Y. Y.; He, S.; Cheng, H.; Xie, Y.; Liu, Q. H.; Jiang, Y.; Wu, Z. Y.; et al. Probing Nucleation Pathways for Morphological Manipulation of Platinum Nanocrystals. *J. Am. Chem. Soc.* **2012**, *134*, 9410−9416.
(90) Li, H.; Li, L.; Pedersen, A.; Gao, Y.; Khetrapal, N.; Jonsson, H.; Zeng, X. C. Magic-Number Gold Nanoclusters with Diameters from 1 to 3.5 nm: Relative Stability and Catalytic Activity for CO Oxidation. *Nano Lett.* **2015**, *15*, 682−688.
(91) Negishi, Y.; Nakazaki, T.; Maloa, S.; Takano, S.; Niihori, Y.; Kurashige, W.; Yamazoe, S.; Tsukuda, T.; Hakkinen, H. A Critical Size for Emergence of Nonbulk Electronic and Geometric Structures in Dodecanethiolate-Protected Au Clusters. *J. Am. Chem. Soc.* **2015**, *137*, 1206−1212.

## Recommended by ACS

**Micro/Nanostructural Analyses of Efficient and Stable Perovskite Solar Cells via KF Doping**

Jiheon Lim, Byungwoo Park, *et al.*
DECEMBER 27, 2022
ACS APPLIED ENERGY MATERIALS
READ

**Improved Alkaline Hydrogen Oxidation on Strain-Modulated Pt Overlayers at Ordered Intermetallic Pt–Sb Cores**

Tianyao Gong, Anthony Shoji Hall, *et al.*
DECEMBER 22, 2022
ACS ENERGY LETTERS
READ

**Mechanistic Understanding of the Electrocatalytic Nitrate Reduction Activity of Double-Atom Catalysts**

Nadaraj Sathishkumar and Hsin-Tsung Chen
JANUARY 09, 2023
THE JOURNAL OF PHYSICAL CHEMISTRY C
READ

**Understanding Structural Incorporation of Oxygen Vacancies in Perovskite Cobaltite Films and Potential Consequences for Electrocatalysis**

Lei Jin, Chun-Lin Jia, *et al.*
NOVEMBER 29, 2022
CHEMISTRY OF MATERIALS
READ

**Get More Suggestions >**


https://doi.org/10.1021/jacs.2c10814
*J. Am. Chem. Soc.* XXXX, XXX, XXX−XXX